processes

MDPI

*Article*

# Influence of Rotation and Viscosity on Parallel Rolls of Electrically Conducting Fluid

**G. Srinivas [1], Y. Rameshwar [2] and D. Laroze [1,*]**

[1] Instituto de Alta Investigación, Universidad de Tarapacá, Casilla 7D, Arica 1000000, Chile; gsrinivas@academicos.uta.cl
[2] Department of Mathematics, University College of Science, Osmania University, Hyderabad 500007, India; rameshwar@osmania.ac.in
* Correspondence: dlarozen@academicos.uta.cl

**Abstract:** Rayleigh–Bénard convection is a fundamental fluid dynamics phenomenon that significantly influences heat transfer in various natural and industrial processes, such as geophysical dynamics in the Earth's liquid core and the performance of heat exchangers. Understanding the behavior of conductive fluids under the influence of heating, rotation, and magnetic fields is critical for improving thermal management systems. Utilizing the Boussinesq approximation, this study theoretically examines the nonlinear convection of a planar layer of conductive liquid that is heated from below and subjected to rotation about a vertical axis in the presence of a magnetic field. We focus on the onset of stationary convection as the temperature difference applied across the planar layer increases. Our theoretical approach investigates the formation of parallel rolls aligned with the magnetic field under free–free boundary conditions. To analyze the system of nonlinear equations, we expand the dependent variables in a series of orthogonal functions and express the coefficients of these functions as power series in a parameter $\epsilon$. A solution for this nonlinear problem is derived through Fourier analysis of perturbations, extending to $O(\epsilon^8)$, which allows for a detailed visualization of the parallel rolls. Graphical results are presented to explore the dependence of the Nusselt number on the Rayleigh number ($R$) and Ekman number ($E$). We observe that both the local Nusselt number and average Nusselt number increase as the Ekman number decreases. Furthermore, the flow appears to become more deformed as $E$ decreases, suggesting an increased influence of external factors such as rotation. This deformation may enhance mixing within the fluid, thereby improving heat transfer between different regions.

**Keywords:** magnetohydrodynamics; electrically conducting fluid; nonlinear convection; parallel rolls



**Citation:** Srinivas, G.; Rameshwar, Y.; Laroze, D. Influence of Rotation and Viscosity on Parallel Rolls of Electrically Conducting Fluid. *Processes* **2024**, *12*, 1882. https://doi.org/10.3390/pr12091882

Academic Editor: Blaž Likozar

Received: 16 July 2024
Revised: 21 August 2024
Accepted: 28 August 2024
Published: 2 Spetember 2024



## 1. Introduction

The magneto-convection issue explored in this paper is motivated by research into the magnetohydrodynamics of the Earth's outer core, which involves the behavior of liquid metals. The flow of electric current across a magnetic field is associated with a body force called the Lorentz force, which influences the fluid flow. As the strength of the magnetic field increases, the Lorentz forces become more dominant compared to the Coriolis force. Given that convection in a rotating and magnetized environment requires a delicate balance of forces, interpreting the results of these models can be quite complex. The geodynamo functions at a low Ekman number ($E$), as this condition is pertinent to geophysical scenarios. Likewise, the growth rate of the parallel rolls remains unaffected by the magnetic field strength ($\Lambda$). When $\Lambda$, the absence of a magnetic field means there is no preferential horizontal direction, resulting in a horizontally isotropic layer that corresponds to the $\Lambda$-independent parallel mode. Instabilities that can develop in a rapidly rotating magnetohydrodynamic system, such as the Earth's core, are often regarded as essential to dynamo theory. This area of research examines how the magnetic field is preserved within the system even in the presence of Ohmic dissipation.

In recent years, notable progress has been made in the creation of dynamos driven by convection. Chendrasekhar [1] examined the linear stability of the layer under the simultaneous action of rotation and magnetic field when both the angular velocity ($\overrightarrow{\Omega}$) and applied magnetic field ($\overrightarrow{B_0}$) are vertically aligned and the boundaries are stress-free. The numerical results indicated that if the Taylor number ($T$) is fixed and Chandrasekhar number ($Q$) increases from zero, the critical Rayleigh number ($R_c$) remains constant until $Q$ reaches a certain value before decreasing. When $Q$ is increased further, $R_c$ decreases, reaching a minimum before increasing again. Roberts and Jones [2] examined how convection begins when the temperature difference across the layer is increased, focusing on the planform and time-dependent behavior of small amplitude convection. Their analysis was guided by a similar study that used specific boundary conditions for illustration. Eltayeb [3] studied the linear stability of a rotating and electrically conducting viscous layer in the Rayleigh–Bénard system with a uniform magnetic field, applying the Boussinesq approximation. He considered several orientations of the magnetic field and rotation axes under various surface conditions. For example, when the magnetic field is horizontal and the rotation is vertical, the rolls align parallel to the magnetic field, provided that the field is weak enough. Childress and Soward [4] presented a hydromagnetic dynamo by examining Bénard convection between rotating parallel planes. Their approach was based on an asymptotic expansion involving two spatial scales, which is suitable for scenarios with large Taylor numbers. Soward [5] has discussed various models of thermal convection in rapidly rotating fluids permeated by strong magnetic fields. Braginsky [6] highlighted the crucial influence of nonuniform rotation in the core. He analyzed small oscillations in electrically conducting fluid affected by magnetic, buoyancy (Archimedean), and Coriolis forces, incorporating Ohmic diffusion to reflect conditions similar to those in the Earth's fluid core. Glatzmaier and Roberts [7] developed and analyzed the first three-dimensional self-consistent numerical solution of the MHD equations, which model thermal convection and magnetic field generation in a rotating spherical fluid shell with a conducting solid inner core. Their results demonstrate a self-sustaining dynamo that can sustain a magnetic field for three different magnetic diffusion times. Jones and Roberts [8] investigated three-dimensional convection-driven dynamos through numerical simulations. Their study uncovered a rich variety of dynamical behaviors that necessitate systematic examination. They focused on both the kinematic and magnetically saturated regimes, proposing a simplified model of the dynamo mechanism. Furthermore, they analyzed the influence of the parameters $R$ and $E$ and the diffusivity ratio $q$ on the dynamo, while also considering the significance of the Taylor constraint in low $E$ convection-driven dynamos. Their results included a snapshot of the flow in the (y,z) plane, revealing a strong correlation between vertical velocity and temperature, as anticipated. Taylor [9] has discussed the influence of magnetic force on the behavior of a rotating incompressible conducting fluid. Soward [10] studied weakly nonlinear convection in Braginsky's model. Geiger and Busse [11] studied the removal of the degeneracy of the patterns of convective motion in a spherically symmetric fluid shell by the effects of rotation. Matthews [12] investigated simple steady flows generated by thermal convection to determine which of them can generate a magnetic field through dynamo action. Kono and Robert [13] described ways of avoiding ambiguity and presented a preferred definition of the $R$ that is particularly well suited for geodynamo simulations. Cattaneo and Hughes [14] studied dynamo processes in a convective layer of Boussinesq fluid rotating about the vertical, and measured the average electromotive force using an externally imposed uniform field. Roberts and Kono [15] presented a new method for evaluating the total energy release. They showed that the gravitational source that stirs the fluid core is less than 30 percent of the total gravitational energy released through the contraction of the Earth as it cools. Tilgner [16] presented numerical simulations of dynamos in rotating Rayleigh–Bénard convection in plane layers.

Earlier research suggests that further investigation is needed into the relationship between the heat transfer rates and control parameters associated with magnetohydro-

dynamic stability. There is also potential for studying flow visualization in electrically conducting fluids rotating about a vertical axis under the influence of a magnetic field.

The current study is particularly relevant to the research conducted by Roberts and Jones [2], which examined the onset of convection. This model involves a vertically rotating Rayleigh–Bénard layer of electrically conducting fluid that generates a magnetic field ($(\overrightarrow{B_0})$) in the horizontal direction. We analytically solve the nonlinear governing equations using the perturbation method proposed by Kuo [17], computing approximate solutions for the dependent variables up to $O(\epsilon^8)$ with free–free boundary conditions. The flow behavior in our dynamo models with stress-free boundary conditions closely resembles that observed with rigid boundary conditions. Our investigation centers on the onset of convection and assesses how various parameters influence fluid flow, temperature distribution, and heat transfer rates. To visualize the fluid flow, temperature distribution, and heat transfer, we utilize the streamline, isotherm, and heatline concepts initially introduced by Kimura and Bejan [18]. Recent studies, such as that by Rameshwar et al. [19], have performed nonlinear analysis of cross-rolls in electrically conducting fluids subjected to an applied magnetic field with rotation. Khedher et al. [20] explored the effects of heating and magnetohydrodynamics (MHD) on the periodic behavior of current density and heat transfer amplitude in electrically conducting fluids. Shuguang et al. [21] analyzed heat transfer in the MHD stagnation point flow of a Maxwell nanofluid over a rotating porous disk, noting that the rotating disk phenomenon leads to the formation of a circular arc at every point on the disk during uniform rotation about an axis. Additionally, Shamshuddin et al. [22] investigated entropy generation in the flow of a tangent hyperbolic magnetized hybrid nanofluid over a stretchable rotating disk, incorporating physical effects such as Ohmic dissipation, nonlinear thermal radiation, heat dissipation, and entropy analysis. Taghreed et al. [23] numerically assessed the combined influence of the wedge angle and melting energy transfer on the flow of tangent hyperbolic magnetohydrodynamic (MHD) nanofluid across a permeable wedge, and also examined the effects of thermal radiation and heat source/sink on the flow of tangent hyperbolic nanofluid (THNF). In their research, Ramanuja et al. [24] examined the steady-state behavior of an electrically conducting and compressible fully developed viscous Jeffrey fluid flowing through infinitely parallel porous vertical microchannels and subjected to a transverse magnetic field. Their study modeled the fluid dynamics using the Navier–Stokes equations combined with energy conservation principles, enabling a detailed analysis of the flow characteristics and thermal behavior under these specific conditions. Qianqian Tang et al. [25] addressed the challenge of enhancing the thermal storage stability of nanosuspension concentrates (SC) derived from low-melting-point pesticides. Their study focused on the preparation of a 25 wt% pyraclostrobin nanosuspension concentrate using a water-based grinding technique, with pyraclostrobin serving as the primary raw material. Jun-Xia Li et al. [26] reported the synthesis of two cobalt(II) complexes via a solvothermal reaction using cobalt chloride hexahydrate and triclopyr acetic acid. Single-crystal X-ray diffraction analysis indicated that both complexes crystallized in the triclinic system, specifically within a defined space group. Yun-Long Wu et al. [27] explored metal–organic framework (MOF)-supported metal nanoparticle (MNP) composites (MNPs@MOFs), which leverage the synergistic effects of both materials. They outlined four main synthesis strategies for these composites: ship-in-the-bottle, bottle-around-the-ship, one-pot, and sandwich assembly. Their review summarizes recent developments in these methods for designing and fabricating various MNPs@MOFs composites.

This version provides a clearer structure and emphasizes the significance of the research questions in relation to the introduction:

- How does the rotation speed of the electrically conducting fluid affect the onset of convection in a vertically oriented Rayleigh–Bénard layer?
- What role do control parameters such as fluid viscosity and thermal conductivity play in the stability of magnetohydrodynamic convection?
- How can the streamline, isotherm, and heatline visualization techniques enhance our understanding of flow dynamics and heat transfer in MHD systems?

- What are the implications of entropy generation in the flow of magnetized hybrid nanofluids over rotating disks with regard to energy efficiency in engineering applications?

This research work is organized as follows: Section 2 provides the magnetohydrodynamic equations in the Boussinesq approximation for the description of the flow; Section 3 presents the linear stability analysis; the method of solution is discussed in Section 4; Section 5 presents the derivation of approximate solutions; analytical approximate expressions for $Nu$ are obtained in Section 6; the patterns of streamlines and isotherms are presented in Section 7; Section 8 deals with the heatfunction and heatline patterns; and Section 9 deals with entropy generation. Finally, the conclusions are provided in Section 10.

## 2. Mathematical Model

Electrically conducting fluids of uniform density are positioned in infinite horizontal layers that rotate about the vertical ($OZ$) axis with an angular velocity expressed as $\vec{\Omega}(=\Omega\vec{1_z})$. A uniform magnetic field $\vec{B_0}(=B_0\vec{1_y})$ is assumed to be applied in the horizontal direction in the presence of uniform gravitational field $\vec{g}$ $(=g\vec{1_z})$ (Figure 1). The momentum equation neglects inertial forces as compared to Coriolis forces. This consideration arises from the assumption of a large Prandtl number ($Pr$). The mathematical equations for the model, based on the Boussinesq approximation, are presented as follows [2]:

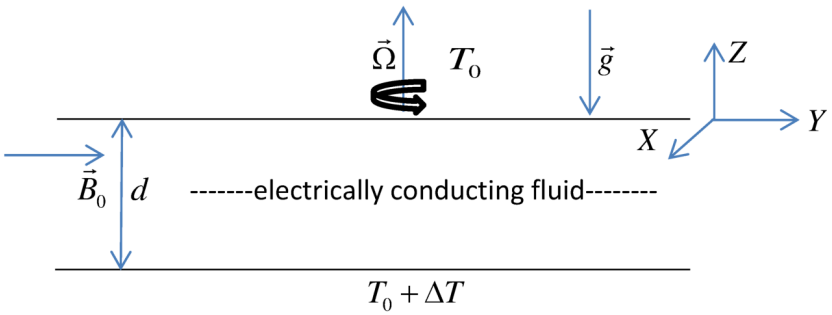


**Figure 1.** Schematic diagram of the physical system.

$$2\vec{\Omega}\rho_0 \times \vec{V'} = -\nabla' P' + \vec{J'} \times \frac{\vec{B'}}{\mu_m} + \vec{g}\alpha\rho_0\, T' + \mu\nabla'^2\vec{V'}, \tag{1}$$

$$\frac{\partial \vec{B'}}{\partial t'} = \nabla' \times (\vec{V'} \times \vec{B'}) + \eta\nabla'^2\vec{B'}, \tag{2}$$

$$\frac{\partial T'}{\partial t'} + \vec{V'} \cdot (\nabla' T') = \kappa\nabla'^2 T', \tag{3}$$

$$\nabla' \cdot \vec{B'} = 0, \tag{4}$$

$$\nabla' \cdot \vec{V'} = 0, \tag{5}$$

where $\vec{J'} = \nabla' \times \vec{B'}$ is the dimensional electric current density. To make Equations (1)–(4) non-dimensional, the following scale parameters are taken into consideration [2]:

$$X = \frac{1}{d}X',\ Y = \frac{1}{d}Y',\ Z = \frac{1}{d}Z',\ t = \frac{\eta}{d^2}t',\ u = \frac{d}{\eta}u',$$
$$v = \frac{d}{\eta}v',\ w = \frac{d}{\eta}w', T = \frac{T'}{\beta d}, B = \frac{1}{B_0}B', p = \frac{1}{2\Omega\rho_0\eta}p'.$$

Equations (1)–(4) then take the following dimensionless form:

$$\vec{1_Z} \times \vec{V} = -\nabla p + \Lambda\vec{J} \times \vec{B} + qR\, T\vec{1_Z} + E\nabla^2\vec{V}, \tag{6}$$

$$\frac{\partial \vec{B}}{\partial t} = \nabla \times (\vec{V} \times \vec{B}) + \nabla^2 \vec{B}, \tag{7}$$

$$\frac{\partial T}{\partial t} + \vec{V} \cdot (\nabla T) = q \nabla^2 T. \tag{8}$$

$$\nabla \cdot \vec{V} = 0, \tag{9}$$

$$\nabla \cdot \vec{B} = 0, \tag{10}$$

where $\vec{J} = \nabla \times \vec{B}$. Equations (6)–(10) are employed to examine the linear stability of a static state:

$$\vec{V}_s = \vec{0}, \ \ \vec{B}_s = \vec{1}_Y, \ \ T_s = -Z. \tag{11}$$

After perturbation, these variables are expressed as dependent variables, provided by

$$\vec{V} = \vec{V}_s + \vec{V}^*, \ \ \vec{B} = \vec{B}_s + \vec{b}^*, \ \ \theta = T_s + \frac{\theta^*}{q}. \tag{12}$$

In the following, the asterisk symbol will be removed for simplicity in the analysis below, and the perturbed dimensionless equations become

$$E\nabla^4 w - \frac{\partial w_Z}{\partial Z} + qR\nabla_h{}^2\theta + \Lambda \frac{\partial}{\partial X}\nabla^2 b_Z = \Lambda \vec{1}_Z \cdot \nabla \times \{\nabla \times [(\nabla \times \vec{b}) \times \vec{b}]\}, \tag{13}$$

$$\left(\frac{\partial}{\partial t} + \vec{V} \cdot \nabla\right)\theta - q\, w - q\nabla^2\theta = 0, \tag{14}$$

$$\left(\frac{\partial}{\partial t} - \nabla^2\right) b_Z = \frac{\partial w}{\partial X} + \vec{1}_Z \cdot \nabla \times (\vec{V} \times \vec{b}), \tag{15}$$

$$\left(\frac{\partial}{\partial t} - \nabla^2\right) B_Z = \frac{\partial w_Z}{\partial X} + \vec{1}_Z \cdot \nabla \times [\nabla \times (\vec{V} \times \vec{b})], \tag{16}$$

$$E\nabla^2 w_Z + \Lambda \frac{\partial B_Z}{\partial X} + \frac{\partial w}{\partial Z} + \Lambda \vec{1}_Z \cdot \nabla \times \ [(\nabla \times \vec{b}) \times \vec{b}] = 0, \tag{17}$$

where

$$\nabla = \vec{1}_X \tfrac{\partial}{\partial X} + \vec{1}_Y \tfrac{\partial}{\partial Y} + \vec{1}_Z \tfrac{\partial}{\partial Z}, \nabla_h^2 = \tfrac{\partial^2}{\partial X^2} + \tfrac{\partial^2}{\partial Y^2},$$
$$\nabla^2 = \tfrac{\partial^2}{\partial X^2} + \tfrac{\partial^2}{\partial Y^2} + \tfrac{\partial^2}{\partial Z^2}, B_z = (\tfrac{\partial b_y}{\partial X} - \tfrac{\partial b_x}{\partial Y}), w_z = (\tfrac{\partial v}{\partial X} - \tfrac{\partial u}{\partial Y}).$$

Here, $\vec{V} = \vec{V}(u, v, w)$ is the perturbed velocity, $\vec{b} = \vec{b}(b_X, b_Y, b_Z)$ is the perturbed magnetic field and $\theta$ is the perturbed temperature field, $\vec{w} = \vec{w}(w_x, w_y, w_z)$ is the vorticity vector, and the other notations are as explained in the Nomenclature. In Equations (13)–(17), the control physical parameters are as follows: $R = \beta g \alpha d^2 / 2\Omega\kappa$ is the Rayleigh number, accounting for buoyancy; $E = \nu / 2\Omega d^2$ is the Ekman number, which measures the viscous force against the Coriolis force; and $\Lambda = {B_0}^2 / 2\Omega\eta\mu_m\rho_0$ is the Elsasser number, which measures the magnetic forces against Coriolis force. The fourth parameter, $q = \kappa/\eta$, denotes the ratio of the thermal diffusivity to the magnetic diffusivity.

By removing $\theta, w_Z, b_Z$, and $B_Z$ from the linear section of Equations (13)–(17), we obtain

$$\mathcal{L}w = \mathcal{N}, \tag{18}$$

$$\mathcal{L} = \mathcal{L}_1 + \mathcal{L}_2 + \mathcal{L}_3 + \mathcal{L}_4 + \mathcal{L}_5 + \mathcal{L}_6,$$

and

$$\mathcal{N} = \mathcal{N}_1 + \mathcal{N}_2 + \mathcal{N}_3 + \mathcal{N}_4 + \mathcal{N}_5,$$

where

$$\mathcal{L}_1 = \left(\frac{\partial}{\partial t} - q\nabla^2\right)\left(\frac{\partial}{\partial t} - \nabla^2\right)^2 \frac{\partial^2}{\partial Z^2},$$

$$\mathcal{L}_2 = E^2\left(\frac{\partial}{\partial t} - q\nabla^2\right)\left(\frac{\partial}{\partial t} - \nabla^2\right)^2 \nabla^6,$$

$$\mathcal{L}_3 = 2E\Lambda\left(\frac{\partial}{\partial t} - q\nabla^2\right)\left(\frac{\partial}{\partial t} - \nabla^2\right)\left(\frac{\partial^2}{\partial X^2}\right)\nabla^4,$$

$$\mathcal{L}_4 = \Lambda^2\left(\frac{\partial}{\partial t} - q\nabla^2\right)\left(\frac{\partial^4}{\partial X^4}\right)\nabla^2,$$

$$\mathcal{L}_5 = RqE\left(\frac{\partial}{\partial t} - \nabla^2\right)^2 \nabla^2 {\nabla_h}^2,$$

$$\mathcal{L}_6 = Rq\Lambda\left(\frac{\partial}{\partial t} - \nabla^2\right)\left(\frac{\partial^2}{\partial X^2}\right){\nabla_h}^2,$$

and

$$\mathcal{N}_1 = \left[ER\left(\frac{\partial}{\partial t} - \nabla^2\right)^2 \nabla^2 {\nabla_h}^2 + R\Lambda\left(\frac{\partial}{\partial t} - \nabla^2\right)\left(\frac{\partial^2}{\partial X^2}\right){\nabla_h}^2\right]\left(\vec{V}\cdot\nabla\right)\theta,$$

$$\mathcal{N}_2 = -\left[E\Lambda\left(\frac{\partial}{\partial t} - q\nabla^2\right)\left(\frac{\partial}{\partial t} - \nabla^2\right)\nabla^4\frac{\partial}{\partial X} + \Lambda^2\left(\frac{\partial}{\partial t} - q\nabla^2\right)\left(\frac{\partial^3}{\partial X^3}\right)\nabla^2\right]\vec{1}_Z\cdot\nabla\times\left(\vec{V}\times\vec{b}\right),$$

$$\mathcal{N}_3 = -\left[\Lambda\left(\frac{\partial}{\partial t} - q\nabla^2\right)\left(\frac{\partial}{\partial t} - \nabla^2\right)\left(\frac{\partial^2}{\partial X\partial Z}\right)\right]\vec{1}_Z\cdot\nabla\times\left[\nabla\times(\vec{V}\times\vec{b})\right],$$

$$\mathcal{N}_4 = \left[\Lambda^2\left(\frac{\partial}{\partial t} - q\nabla^2\right)\left(\frac{\partial}{\partial t} - \nabla^2\right)\frac{\partial^2}{\partial X^2}\right]\vec{1}_Z\cdot\nabla\times\nabla\times\left[(\nabla\times\vec{b})\times\vec{b}\right] +$$
$$\left[E\Lambda\left(\frac{\partial}{\partial t} - q\nabla^2\right)\left(\frac{\partial}{\partial t} - \nabla^2\right)^2\nabla^2\right]\vec{1}_Z\cdot\nabla\times\nabla\times\left[\left(\nabla\times\vec{b}\right)\times\vec{b}\right],$$

$$\mathcal{N}_5 = -\left[\Lambda\left(\frac{\partial}{\partial t} - q\nabla^2\right)\left(\frac{\partial}{\partial t} - \nabla^2\right)^2\frac{\partial}{\partial Z}\right]\vec{1}_Z\cdot\nabla\times\left[\left(\nabla\times\vec{b}\right)\times\vec{b}\right].$$

The stress-free boundary conditions are specified on the horizontal planes at $Z = 0$ and $Z = 1$. Because the surface temperature is kept constant, we have

$$\theta = 0 \text{ on } Z = 0 \text{ and } Z = 1 \text{ for every } X, Y. \tag{19}$$

At the boundaries, the standard component of velocity should also be equal to zero, i.e.,

$$w = 0 \text{ on } Z = 0 \text{ and } Z = 1 \text{ for every } X, Y. \tag{20}$$

The conditions in (19) and (20) are independent of any type of boundaries. The stress-free boundary conditions are considered; hence, we have the following:

$$\frac{\partial^2 w}{\partial Z^2} = \frac{\partial w_z}{\partial Z} = 0 \text{ on } Z = 0 \text{ and } Z = 1 \text{ for every } X, Y, \tag{21}$$

$$B_X = B_Y = \frac{\partial B_Z}{\partial Z} = 0 \text{ on } Z = 0 \text{ and } Z = 1 \text{ for every } X, Y. \tag{22}$$

## 3. Linear Stability Analysis

At the onset of convection, the system has only slight disturbances, causing the nonlinear terms to be considerably smaller than the linear terms. As a result, nonlinear contributions from Equation (18) are neglected. We obtain the linear differential equation, with the solution being $\mathcal{L}w = 0$; thus,

$$\left[\left(\frac{\partial}{\partial t} - q\nabla^2\right)\left(\frac{\partial}{\partial t} - \nabla^2\right)^2 \frac{\partial^2}{\partial Z^2} + E^2\left(\frac{\partial}{\partial t} - q\nabla^2\right)\left(\frac{\partial}{\partial t} - \nabla^2\right)^2 \nabla^6 + R\left(qE\left(\frac{\partial}{\partial t} - \nabla^2\right)^2 \nabla^2 {\nabla_h}^2\right)\right] w = 0. \tag{23}$$

The resulting equation is linear. We define $w(X, Y, Z, t) = W(Z)e^{ikX+iaY+\lambda t}$, where $k$ and $a$ are constant wavenumbers. The modes with $k = 0$ are called parallel rolls, which are independent of the magnetic field strength ($\Lambda$). When $\Lambda = 0$, the magnetic force does not impart a preferred horizontal direction. The growth rate ($\lambda$) is a constant that remains real for parallel rolls, indicating that they are never overstable [2]. The linear stability analysis is explored by replacing $w(Y, Z, t) = W(Z)e^{iaY+\lambda t}$ in the linearized equation $\mathcal{L}w = 0$, using the normal mode analysis.

*Stationary Convection*

Equation (23) provides the Rayleigh number for stationary mode by taking $\lambda = 0$, and is provided by

$$R = \frac{\pi^2 + d_2^3 E^2}{a^2 E},$$

where $d_2 = a^2 + \pi^2$. Figure 2 displays $R$ as a function of $a$ for various Ekman number ($E$) values. It can be seen that as $E$ decreases, the critical value $R_{cs}$ also diminishes. This suggests that a lower Ekman number ($E$) contributes to a destabilizing effect on the flow. The critical value of $R$ ($R_{cs}$) is found by setting $\partial R/\partial a^2 = 0$. The critical wavenumber is provided by $a^2 = {a^2}_{cs} = 2\pi^2$, and the critical value of ($R_{cs}$) of $R$ for stationary convection is defined as

$$R_{cs} = \frac{27\, E^2 \pi^4 + 1}{2E}.$$

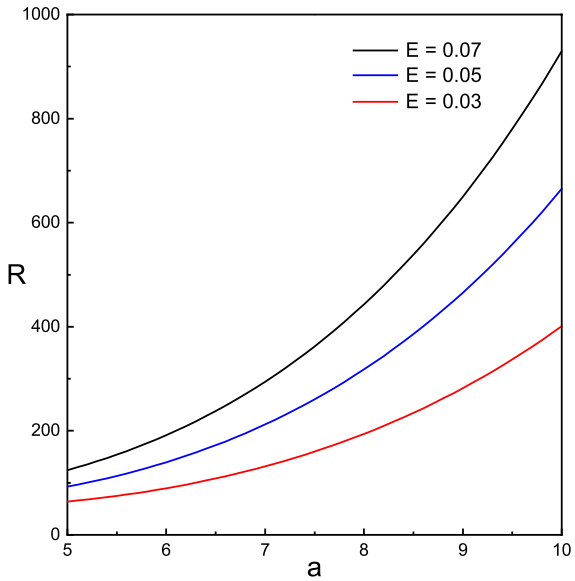


**Figure 2.** Dependence of $R$ on $a$ for $E = 0.03, 0.05$ and $0.07$.

## 4. Method of Solution

According to Kuo [17], a solution can be achieved for the nonlinear system of equations by means of two expansions. First, the dependent variables are expanded in a series of orthogonal functions. Second, the coefficients associated with these functions are expanded in a power series of a parameter $\epsilon < 1$ as

$$\epsilon^2 = \frac{R - R_{cs}}{R}. \tag{24}$$

The solutions for Equations (13)–(17) are represented as follows:

$$f = \epsilon f_1 + \epsilon^2 f_2 + \epsilon^3 f_3 + \epsilon^4 f_4 + \epsilon^5 f_5 + \epsilon^6 f_6 + \cdots, \tag{25}$$

where

$$f = f(v, w, \theta, b_Y, b_Z, w_Z, B_Z).$$

The value of $R$ according to Equation (24) is expressed as

$$R = \frac{R_{cs}}{1 - \epsilon^2}, \tag{26}$$

and is either expanded in a power series in $\epsilon$ or the finite formula is applied as

$$R = R_{cs} + R_{os}(\epsilon^2 + \epsilon^4 + \epsilon^6 + \ldots + \epsilon^{2s}), \tag{27}$$

where

$$R_{os} = \frac{R_{cs}}{1 - \epsilon^{2s}}, \quad s = 1, 2, 3 \ldots\ldots \tag{28}$$

By introducing Equations (25) and (27) into Equation (13), the following different-order equations are obtained:

$$O(\epsilon) : (\mathcal{L}_1 + \mathcal{L}_2 + \mathcal{L}_3 + \mathcal{L}_4)w_1 + R_{cs}(\mathcal{L}_5 + \mathcal{L}_6)w_1 = 0, \tag{29}$$

$$O(\epsilon^2) : (\mathcal{L}_1 + \mathcal{L}_2 + \mathcal{L}_3 + \mathcal{L}_4)w_2 + R_{cs}(\mathcal{L}_5 + \mathcal{L}_6)w_2 = 0. \tag{30}$$

$$\begin{aligned} O(\epsilon^3) : (\mathcal{L}_1 + \mathcal{L}_2 + \mathcal{L}_3 + \mathcal{L}_4)w_i + R_{cs}(\mathcal{L}_5 + \mathcal{L}_6)w_i + R_{os}(\mathcal{L}_5 + \mathcal{L}_6)w_{i-2} \\ = R_{cs}\mathcal{N}_1 + \mathcal{N}_2 + \mathcal{N}_3 + \mathcal{N}_4 + \mathcal{N}_5, \text{ for } i = 3. \end{aligned} \tag{31}$$

$$\begin{aligned} O(\epsilon^4) : (\mathcal{L}_1 + \mathcal{L}_2 + \mathcal{L}_3 + \mathcal{L}_4)w_i + R_{cs}(\mathcal{L}_5 + \mathcal{L}_6)w_i + R_{os}(\mathcal{L}_5 + \mathcal{L}_6)w_{i-2} \\ + R_{os}(\mathcal{L}_5 + \mathcal{L}_6)w_{i-4} = (R_{cs} + R_{os})\mathcal{N}_1 + \mathcal{N}_2 + \mathcal{N}_3 + \mathcal{N}_4 + \mathcal{N}_5, \text{ for } i = 4, 5. \end{aligned} \tag{32}$$

In general,

$$\begin{aligned} (\mathcal{L}_1 + \mathcal{L}_2 + \mathcal{L}_3 + \mathcal{L}_4)w_i + R_{cs}(\mathcal{L}_5 + \mathcal{L}_6)w_i + R_{os}(\mathcal{L}_5 + \mathcal{L}_6)w_{i-2} \\ + R_{os}(\mathcal{L}_5 + \mathcal{L}_6)w_{i-4} = (R_{cs} + 2R_{os})\mathcal{N}_1 + \mathcal{N}_2 + \mathcal{N}_3 + \mathcal{N}_4 + \mathcal{N}_5, \text{ for } i \geq 6. \end{aligned} \tag{33}$$

Here, the linear operators in $\mathcal{L}_i$, $i = 1, 2, 3, 4, 5, 6$ and the nonlinear terms in $\mathcal{N}_i$, $i = 1, 2, 3, 4, 5$ are the functions of $v_i$, $w_i$, $\theta_i$, $b_{Y_i}$ and $b_{Z_i}$. Each $v_i$, $w_i$ and $\theta_i$ must satisfy the boundary conditions in Equations (19)–(21). In addition, $\theta_i$, $b_{Y_i}$ and $b_{Z_i}$ are evaluated from $v_i$ and $w_i$ using an auxiliary equation derived from the Equations (31)–(33). The spectral equation for the temperature is provided by

$$\left(\frac{\partial}{\partial t} - \nabla^2\right)\theta_1 = q w_1, \tag{34}$$

$$\left(\frac{\partial}{\partial t}-\nabla^2\right)\theta_2+(\overrightarrow{V}_1.\nabla)\theta_1=qw_2. \tag{35}$$

In general,

$$\left(\frac{\partial}{\partial t}-\nabla^2\right)\theta_i+\sum_{l=1}^{i-1}(\overrightarrow{V}_l.\nabla)\theta_{i-l}=qw_i, \text{ for } \ i\geq 3. \tag{36}$$

Similarly, the equations for the magnetic field are formulated as follows:

$$\left(\frac{\partial}{\partial t}-\nabla^2\right)b_{Y_1}=\frac{\partial v_1}{\partial X}, \tag{37}$$

$$\begin{aligned}\left(\frac{\partial}{\partial t}-\nabla^2\right)b_{Y_i}=&\frac{\partial v_i}{\partial X}+\frac{\partial}{\partial X}\left(v_1b_{X_{i-1}}+\cdots+v_{i-1}b_{X_1}-u_1b_{Y_{i-1}}\cdots+u_{i-1}b_{Y_1}\right)\\&+\frac{\partial}{\partial Z}\left(v_1b_{Z_{i-1}}+\cdots+v_{i-1}b_{Z_1}-w_1b_{Y_{i-1}}\cdots+w_{i-1}b_{Y_1}\right), \text{ for } \ i\geq 2,\end{aligned} \tag{38}$$

$$\left(\frac{\partial}{\partial t}-\nabla^2\right)b_{Z_1}=\frac{\partial w_1}{\partial X}, \tag{39}$$

$$\begin{aligned}\left(\frac{\partial}{\partial t}-\nabla^2\right)b_{Z_i}=&\frac{\partial w_i}{\partial X}-\frac{\partial}{\partial X}\left(u_1b_{Z_{i-1}}+\cdots+u_{i-1}b_{Z_1}-w_1b_{X_{i-1}}\cdots+w_{i-1}b_{X_1}\right)\\&-\frac{\partial}{\partial Y}\left(v_1b_{Z_{i-1}}+\cdots+v_{i-1}b_{Z_1}-w_1b_{Y_{i-1}}\cdots+w_{i-1}b_{Y_1}\right) \text{ for } \ i\geq 2.\end{aligned} \tag{40}$$

## 5. Discussion of the Solution

The approximate solutions for $w, \theta$, $b_Y$, and $b_Z$ are calculated in terms of amplitude. For the case with two free boundaries, the spatial functions associated with the different modes $w, \theta$, $b_Y$, and $b_Z$ are represented by sine and cosine functions. Hence, from Equations (29), (34), (37) and (39), the first order of the approximate solution is provided by

$$\begin{aligned}w_1&=A_1\cos aY\sin\pi Z,\\v_1&=\frac{1}{a^2}\frac{\partial^2 w_1}{\partial z\partial y},\\\theta_1&=\frac{q}{\pi^2+a^2}A_1\cos aY\sin\pi Z,\\b_{Y_1}&=0,\\b_{Z_1}&=0,\end{aligned} \tag{41}$$

where the amplitude $A_1$ is determined from the nonlinear terms. Generally, the terms in Equation (25) may be written as

$$w_i=A_i\cos aY\sin\pi Z+\sum_{p_1,q_1}w^{(i)}_{p_1q_1}\cos p_1aY\sin q_1\pi Z, \tag{42}$$

$$v_i=\frac{1}{a^2}\frac{\partial^2 w_i}{\partial z\partial y}, \tag{43}$$

$$\theta_i=\frac{qA_i}{\pi^2+a^2}\cos aY\sin\pi Z+\sum_{p_1,q_1}\theta^{(i)}_{p_1q_1}\cos p_1aY\sin q_1\pi Z, \tag{44}$$

$$b_{Y_i}=0, \tag{45}$$

$$b_{Z_i}=0, \tag{46}$$

where $w_{p_1q_1}^{(i)}$ and $\theta_{p_1q_1}^{(i)}$ are nonlinear functions of the amplitudes $A_1$, $A_2$, $A_3$..... $A_{i-1}$. The unknown functions $w_{p_1q_1}^{(i)}$, $\theta_{p_1q_1}^{(i)}$ (and the amplitudes $A_1$, $A_2$, $A_3$..... $A_{i-1}$) are obtained by substituting Equations (25) and (27) in Equations (13)–(17). We utilize the principle that the coefficients of each power of $\epsilon$ must equal zero.

### 5.1. Evaluation of Amplitude $A_1$

To solve the second-order solutions $w_2$, $\theta_2$, $b_{X_2}$, and $b_{Z_2}$, the nonlinear term $\mathcal{N}$ needs to be calculated. From Equation (30), it is observed that $\mathcal{N} = 0$; this leads to $\mathcal{L}w_2 = 0$ and

$$w_{02}^{(2)} = 0 \text{ and } \theta_{02}^{(2)} = \frac{-q\pi A_1^2}{8\pi^2(\pi^2 + a^2)}. \tag{47}$$

The unknown functions $w_2$, $\theta_2$, $b_{Y_2}$, and $b_{Z_2}$ are obtained from Equations (30), (35), (38) and (40), respectively, and are expressed as follows:

$$\begin{aligned} w_2 &= A_2 \cos aY \sin \pi Z, \\ v_2 &= \frac{1}{a^2}\frac{\partial^2 w_2}{\partial z \partial y}, \\ \theta_2 &= \frac{qA_2}{\pi^2 + a^2} \cos aY \sin \pi Z + {\theta_{02}}^{(2)} {A_1}^2 \sin 2\pi Z, \\ b_{Y_2} &= 0, \\ b_{Z_2} &= 0. \end{aligned} \tag{48}$$

From Equation (31), for $i = 3$, the amplitude $A_1$ is calculated as

$$\begin{aligned} &(\mathcal{L}_1 + \mathcal{L}_2 + R_{cs}\mathcal{L}_5)w_3 + R_{os}\mathcal{L}_5 w_1 \\ &= R_{cs}[Eq(a^2 + 9\pi^2)^3 a^2]\pi\theta_{02}^{(2)} {A_1}^3 \cos aY \sin 3\pi Z \\ &\quad - R_{cs}[Eq(a^2 + \pi^2)^3 a^2]\pi\theta_{02}^{(2)} {A_1}^3 \cos aY \sin \pi Z. \end{aligned} \tag{49}$$

Solving the above equation provides $A_1$, and can be expressed by

$$A_1 = \frac{\sqrt{R_{cs}\,\pi\,\theta_{02}^{(2)} R_{os}\,q}}{R_{cs}\,\pi\,\theta_{02}^{(2)}}. \tag{50}$$

The unknown functions $w_3$ and $\theta_3$ are obtained from Equations (31) and (36), respectively, which are provided by

$$\begin{aligned} w_3 &= A_3 \cos aY \sin \pi Z + w_{13}^{(3)} \cos aY \sin 3\pi Z, \\ v_3 &= \frac{1}{a^2}\frac{\partial^2 w_3}{\partial z \partial y}, \\ \theta_3 &= \frac{qA_3}{\pi^2 + a^2} \cos aY \sin \pi Z + \theta_{11}^{(3)} \cos aY \sin \pi Z \\ &\quad + \theta_{13}^{(3)} \cos aY \sin 3\pi Z + \theta_{02}^{(3)} \sin 2\pi Z, \end{aligned} \tag{51}$$

where

$$w_{13}^{(3)} = \frac{R_{cs}\,Eq\left(9\,\pi^2 + a^2\right)^2 a^2 \pi\,\theta_{02}^{(2)}}{D_{13}}$$

and

$$\theta_{11}^{(3)} = -\frac{\pi\,\theta_{02}^{(2)}}{d_2},$$

$$\theta_{13}^{(3)} = \frac{q^2(9\,\pi^2 + a^2)R_{cs}\,Ea^2\pi\,\theta_{02}^{(2)}}{-9\,q(9\,\pi^2 + a^2)^3\pi^2 - E^2q(9\,\pi^2 + a^2)^6 + R_{cs}\,q^2E(9\,\pi^2 + a^2)^3a^2} - \frac{\pi\,\theta_{02}^{(2)}}{9\,\pi^2 + a^2}.$$

This iterative process is continued to find $A_2$, $A_3$, $A_4$, $A_5$, $A_6$ and the corresponding $w$, $\theta$, $b_X$, $b_Z$.

### 5.2. Evaluation of Amplitudes $A_2$ and $A_3$

Initially, Equation (32) is solved for $i = 4$, i.e.,

$$(\mathcal{L}_1 + \mathcal{L}_2 + R_{cs}\mathcal{L}_5)w_4 + R_{os}\mathcal{L}_5w_2 = (R_{cs} + R_{os})\mathcal{N}_1 + \mathcal{N}_2 + \mathcal{N}_3 + \mathcal{N}_4 + \mathcal{N}_5. \tag{52}$$

The nonlinear terms $\mathcal{N}_i$, $i$ = 1, 2, 3, 4, 5 are determined by utilizing Equations (41), (48) and (51). From the solvability condition of Equation (52), we have $A_2 = 0$. This means that all second-order solution vanish except for $\theta_{02}^{(2)}$, which is shown in Equation (48). Therefore, Equation (52) reduces to

$$\begin{aligned}(\mathcal{L}_1 + \mathcal{L}_2 + R_{cs}\mathcal{L}_5)w_4 + R_{os}\mathcal{L}_5w_2 = {} & K_1{A_1}^4\cos 2aY\sin 4\pi Z \\ & + K_2{A_1}^4\cos 2aY\sin 2\pi Z.\end{aligned} \tag{53}$$

The coefficients $K_1$ and $K_2$ in Equation (53) are functions of $a, E,$ and $q$, while $w_4$, $\theta_4$ are evaluated by Equations (32) and (36) and are provided by

$$\begin{aligned}w_4 = {} & A_4\cos aY\sin\pi Z + w_{24}^{(4)}A_1^4\cos 2aY\sin 4\pi Z \\ & + w_{22}^{(4)}A_1^4\cos 2aY\sin 2\pi Z, \\ v_4 = {} & \frac{1}{a^2}\frac{\partial^2 w_4}{\partial z\partial y},\end{aligned} \tag{54}$$

$$\begin{aligned}\theta_4 = {} & \frac{q}{(a^2 + \pi^2)}A_4\cos aY\sin\pi Z + \theta_{02}^{(4)}A_1A_3\sin 2\pi Z \\ & + \theta_{02}^{(4)}A_1^4\sin 2\pi Z + \theta_{22}^{(4)}A_1^4\cos 2aY\sin 2\pi Z \\ & + \theta_{24}^{(4)}A_1^4\cos 2aY\sin 4\pi Z + \theta_{04}^{(4)}A_1^4\sin 4\pi Z\end{aligned} \tag{55}$$

where

$$w_{24}^{(4)} = 4\,\frac{Eq{d_{24}}^3a^2(R_{cs} + R_{os})}{D_{24}}\left(\frac{1}{2}\,\pi\,\theta_{13}^{(3)} + \frac{1}{4}\,\frac{qav_{13}^{(3)}}{d_2} + \frac{1}{4}\,\frac{q\pi\,w_{13}^{(3)}}{d_2}\right),$$

$$w_{22}^{(4)} = 4\,\frac{Eq{d_{22}}^3a^2(R_{cs} + R_{os})}{D_{22}}\left(-\pi\,\theta_{13}^{(3)} - \frac{1}{4}\,\frac{qav_{13}^{(3)}}{d_2} + \frac{1}{4}\,\frac{q\pi\,w_{13}^{(3)}}{d_2}\right),$$

$$\theta_{02}^{(4)} = -\frac{1}{4}\,\frac{1}{\pi^2}\left(-\frac{1}{2}\,\pi\,\theta_{13}^{(3)} + \frac{1}{4}\,\frac{qav_{13}^{(3)}}{d_2} + \frac{1}{4}\,\frac{q\pi\,w_{13}^{(3)}}{d_2} + \frac{1}{2}\,\pi\,\theta_{11}^{(3)}\right),$$

$$\theta_{04}^{(4)} = -\frac{1}{16}\,\frac{1}{\pi^2}\left(\pi\,\theta_{13}^{(3)} - \frac{1}{4}\,\frac{qav_{13}^{(3)}}{d_2} + \frac{1}{4}\,\frac{q\pi\,w_{13}^{(3)}}{d_2}\right),$$

$$\theta_{22}^{(4)} = \frac{1}{d_{22}}\left(qw_{22}^{(4)} + \pi\,\theta_{13}^{(3)} + \frac{1}{4}\,\frac{qav_{13}^{(3)}}{d_2} - \frac{1}{4}\,\frac{q\pi\,w_{13}^{(3)}}{d_2}\right),$$

$$\theta_{24}^{(4)} = \frac{1}{d_{24}}\left(qw_{24}^{(4)} - \frac{1}{2}\,\pi\,\theta_{13}^{(3)} - \frac{1}{4}\,\frac{qav_{13}^{(3)}}{d_2} - \frac{1}{4}\,\frac{q\pi\,w_{13}^{(3)}}{d_2}\right),$$

and

$$D_{24} = -16\,q(d_{24})^3\pi^2 - E^2q(d_{24})^6 + 4\,R_{cs}\,q^2E(d_{24})^3a^2,$$

$$D_{22} = -4\,q(d_{22})^3\pi^2 - E^2q(d_{22})^6 + 4\,R_{cs}\,q^2E(d_{22})^3a^2,$$
$$d_{22} = 4a^2 + 4\pi^2, d_{24} = 4a^2 + 16\pi^2.$$

To determine the value of $A_3$, the fifth-order equation for $i$ = 5 of Equation (32) is solved, which can be written as follows:

$$(\mathcal{L}_1 + \mathcal{L}_2 + R_{cs}\mathcal{L}_5)w_5 + R_{os}\mathcal{L}_5(w_3 + w_1) = (R_{cs} + R_{os})\mathcal{N}_1. \tag{56}$$

Evaluating $\mathcal{N}_1$ from Equations (41), (48), (51), (54) and (55) we obtain

$$\begin{aligned}\mathcal{N}_1 = {} & D_1A_1^5\cos aY\sin 5\pi Z + D_2A_1^5\cos aY\sin 3\pi Z\\ & + D_3A_1^5\cos 3aY\sin 5\pi Z + D_4A_1^5\cos 3aY\sin 3\pi Z\\ & + D_5A_1^5\cos aY\sin \pi ZZ + D_6A_1^5\cos 3aY\sin \pi Z\\ & + D_7A_1^2A_3\cos aY\sin 3\pi Z + D_8A_1^2A_3\cos aY\sin \pi Z.\end{aligned} \tag{57}$$

In Equation (57), the coefficients $D_i$, $i = 1, 2\ldots, 8$ are the functions of $a, E$, and $q$ ($D_i = D_i\,(a, E, q)$). Thus, $A_3$ is provided by

$$A_3 = \frac{S_1}{S_2}, \tag{58}$$

where

$$S_1 = -R_{os}\,q^2E{d_2}^3a^2A_1$$
$$+Eq{d_2}^3a^2\left(\pi\,\theta_{02}^{(2)}\,w_{13}^{(3)} + \frac{aqv_{22}^{(4)}}{4d_2} + \frac{\pi\,qw_{22}^{(4)}}{4d_2} + \frac{1}{4}\,\pi\,\theta_{22}^{(4)} - \theta_{02}^{(4)}\,\pi\right)$$
$$\times(R_{cs} + R_{os}){A_1}^5,$$

and

$$S_2 = R_{os}\,q^2E{d_2}^3a^2 - Eq{d_2}^3a^2\left(-\pi\,\theta_{02}^{(2)} - \theta_{02}^{(4)}\,\pi\right)(R_{cs} + R_{os}){A_1}^3.$$

The amplitude $A_3$ is determined from the first-, second, third-, fourth-, and fifth-order approximate solutions; $w_5$ and $\theta_5$ are evaluated from Equations (36) and (56), and are provided by

$$\begin{aligned}w_5 = {} & A_5\,\cos aY\sin\pi\,Z + D_9\,{A_1}^3\cos aY\sin 3\,\pi\,Z\\ & + D_{10}\,{A_1}^5\cos aY\sin 3\,\pi\,Z + D_{11}\,{A_1}^2A_3\,\cos aY\sin 3\,\pi\,Z\\ & + D_{12}\,{A_1}^5\cos aY\sin 5\,\pi\,Z + D_{13}\,{A_1}^5\cos 3\,aY\sin 5\,\pi\,Z\\ & + D_{14}\,{A_1}^5\cos 3\,aY\sin 3\,\pi\,Z + D_{15}\,{A_1}^5\cos 3\,aY\sin \pi\,Z,\\ v_5 = {} & \frac{1}{a^2}\frac{\partial^2 w_5}{\partial z\partial y},\\ \theta_5 = {} & \frac{A_5q\,\cos aY\sin\pi\,Z}{d_2} + D_{16}\,{A_1}^3\cos aY\sin 3\,\pi\,Z\\ & + D_{17}\,{A_1}^5\cos aY\sin 3\,\pi\,Z + D_{18}\,{A_1}^2A_3\,\cos aY\sin 3\,\pi\,Z\\ & + D_{19}\,{A_1}^5\cos aY\sin 5\,\pi\,Z + D_{20}\,{A_1}^5\cos 3\,aY\sin 5\,\pi\,Z\\ & + D_{21}\,{A_1}^5\cos 3\,aY\sin 3\,\pi\,Z + D_{22}\,{A_1}^5\cos 3\,aY\sin \pi\,Z\\ & + D_{23}\,{A_1}^2A_3\,\cos aY\sin\pi\,Z + D_{24}\,A_1\,A_4\,\sin 2\,\pi\,Z,\end{aligned} \tag{59}$$

where the coefficients $D_i$, $i = 9, 10\ldots, 24$ are the functions of $a, E$, and $q$ ($D_i = D_i\,(a, E, q)$).

### *5.3. Evaluation of Amplitudes $A_4$, $A_5$, and $A_6$*

Proceeding as above, the sixth-order approximate solutions are obtained from Equations (33) and (36) and are provided by

$$
\begin{aligned}
w_6 &= A_6 \cos aY \sin \pi Z \\
&\quad + \cos 2aY(E_1 \sin 2\pi Z + E_2 \sin 4\pi Z + E_3 \sin 6\pi Z) \\
&\quad + \cos 4aY(E_4 \sin 2\pi Z + E_5 \sin 4\pi Z + E_6 \sin 6\pi Z), \\
v_6 &= \frac{1}{a^2} \frac{\partial^2 w_6}{\partial z \partial y}, \\
\theta_6 &= \frac{qA_6}{\pi^2 + a^2} \cos aY \sin \pi Z \\
&\quad + \cos 2aY(E_7 \sin 2\pi Z + E_8 \sin 4\pi Z + E_9 \sin 6\pi Z) \\
&\quad + \cos 4aX(E_{10} \sin 2\pi Z + E_{11} \sin 4\pi Z + E_{12} \sin 6\pi Z) \\
&\quad + E_{13} \sin 2\pi Z + E_{14} \sin 4\pi Z + E_{15} \sin 6\pi Z. \qquad (60)
\end{aligned}
$$

In Equation (60), the coefficients $E_i$ $(i = 1, 2 \ldots, 15)$ are functions of $a$, $E$, and $q$ ($E_i = E_i$ $(a, E, q)$). The solution of the sixth-order equation provides $A_4 = 0$. The above solution plays an important role in the calculation of $A_5$, which can be found by solving the seventh order of Equation (33). The computation becomes more tedious as the order of $\epsilon$ increases. Proceeding as above, $A_6 = 0$ can be obtained; thus, it can be observed that $A_2 = A_4 = A_6 = 0$.

## 6. Natural Convective Heat Transport

The local Nusselt number ($N_L$), which represents the heat transfer coefficient, is defined as follows [18–31]:

$$N_L = \frac{\partial T}{\partial n}, \qquad (61)$$

where $\frac{\partial}{\partial n}$ stands for dimensionless derivation of the normal direction on the plane. The average Nusselt number $Nu$ for heat transfer, which is independent of the axial coordinate $Z$, can be expressed as follows:

$$Nu = \overline{wT} - \frac{\partial \overline{T}}{\partial Z}. \qquad (62)$$

In this context, the overbar indicates that we are using the mean value of the convective heat transfer coefficient across the horizontal plane. Using Equation (62), we obtain $Nu$ by integrating the expression over the range of interest, such as on the boundary, with $Z = 0$ [30].

$$Nu = \frac{1}{L} \int_0^L \left( WT - \frac{\partial T}{\partial Z}|_{Z=0} \right) dY, \qquad (63)$$

where $L$ denotes the normalized horizontal cell width.

### *6.1. Local Nusselt Number ($N_L$)*

The influence of the Rayleigh number and Ekman number on heat transfer across a boundary is analyzed through the local Nusselt number. Figure 3a,b displays the local Nusselt number distributions along the heated bottom wall for different Rayleigh and Ekman numbers. In Figure 3a, it is evident that an increase in the Rayleigh number leads to a higher heat transfer rate, which is attributed to improved fluid flow. At lower Rayleigh numbers the convection is minimal and heat transfer is primarily governed by conduction, resulting in the presence of small spikes in the Nusselt number. Figure 3b shows how the local Nusselt number varies along the bottom wall for various Ekman numbers while the Rayleigh number is kept constant at $R = 8R_{cs}$. This demonstrates how changes in the Ekman number affect the local heat transfer performance, complementing the findings from varying Rayleigh numbers. This phenomenon can be attributed to the reduced viscous damping effects at lower Ekman numbers, which allow for more vigorous fluid motion and enhanced convective heat transfer. As the Ekman number decreases, the flow becomes

less influenced by viscous forces, facilitating stronger thermal gradients and increased heat flux across the fluid layer.

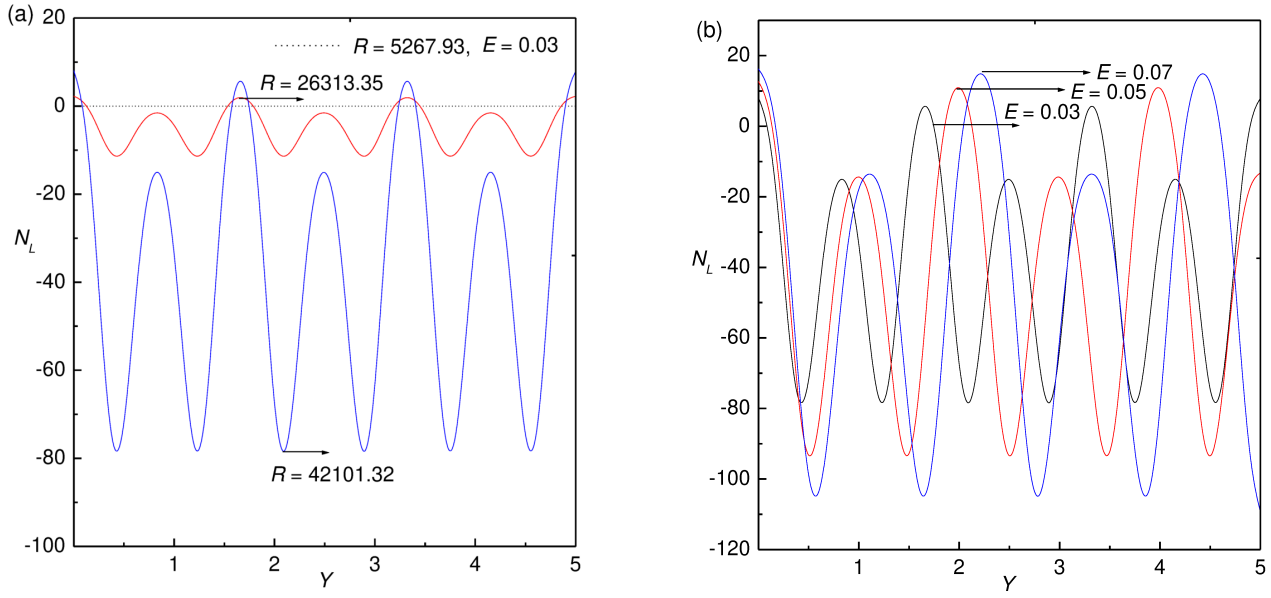


**Figure 3.** Variation of $N_L$ with respect to Y: (**a**) $E = 0.03$, $R_{cs} = 5262.664915$, and $q = 0.01$ for different $R$; (**b**) $R = 8R_{cs}$ and $q = 0.01$ for different $E$.

### *6.2. Average Nusselt Number (Nu)*

The average Nusselt number ($Nu$) can be calculated to characterize the overall heat transfer behavior in a system. For this analysis, we consider $Nu^{(2)}(s = 1)$, $Nu^{(4)}(s = 2)$, and $Nu^{(6)}(s = 3)$, to represent the second-, fourth-, and sixth-order approximations of the Nusselt number, respectively; $Nu^{(2)}$ is calculated, and is provided by

$$Nu^{(2)} = 1 + 0.787\,\frac{1}{\pi R_{cs}} \cdot \sqrt{\frac{(27\,E^2\pi^4 - 2\,R_{cs}\,qE + 1)R_{cs}\,q}{E}}. \tag{64}$$

Due to the lengthy expression of $A_3$ and $A_5$, the approximations for $Nu^{(4)}$ and $Nu^{(6)}$ are lengthy, and are not included here to conserve space.

Figure 4 illustrates the influence of the Rayleigh number $R$ on the Nusselt number $Nu$ for various Ekman numbers ($E$). From the figure, it can be seen that at low Rayleigh numbers the average Nusselt number is roughly equal to the Rayleigh number; however, when $R$ surpasses $10^4$, the mean Nusselt number shows an increasing trend with rising Rayleigh numbers. Additionally, a transition from conduction to convection heat transfer occurs beyond $R = 10^4$. It is important to note that the heat transfer coefficient is influenced not only by the Rayleigh number but also by the Ekman number, with the average Nusselt number rising as the Ekman number decreases. If the Ekman number is low, then the viscous force is weak, while if the Ekman number is large, then the viscous force is strong. Therefore, the combination of the largest Rayleigh number and smallest Ekman number in the selected region provides the maximum value of the average Nusselt number. Figure 5 shows the plot of energy versus $R/R_{cs}$ for several values of $E$. We find that the potential energy is almost constant for all combinations of the Rayleigh number and Ekman number, while the kinetic energy increases as the value of the Ekman number decreases. This is because a lower Ekman number reduces viscous forces and increases kinetic energy.

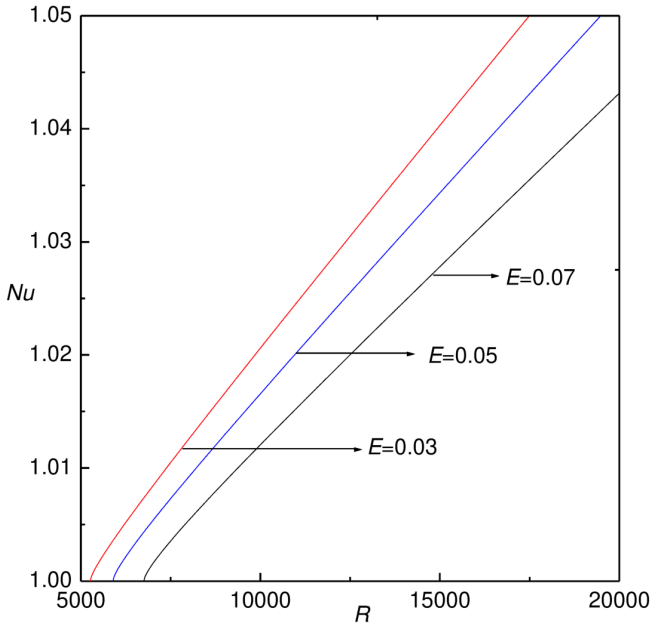


**Figure 4.** Dependence of $Nu$ on $R$ for $E = 0.03, 0.05, 0.07$, and $q = 0.01$.

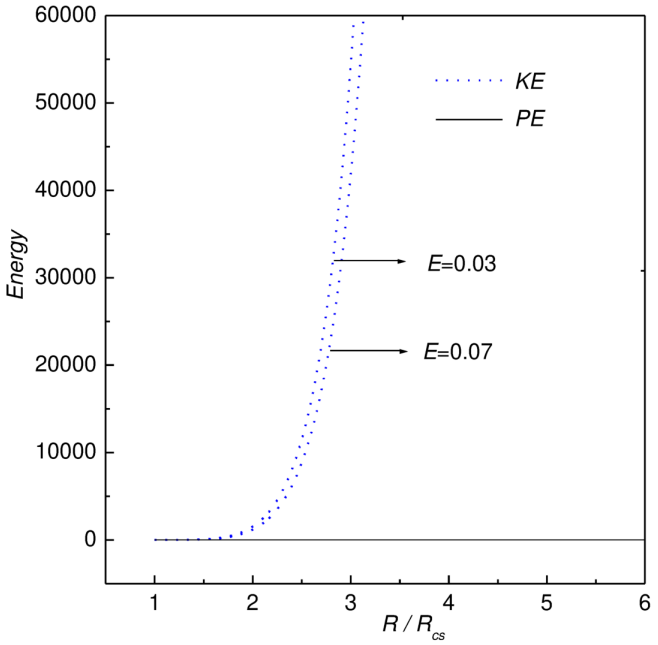


**Figure 5.** Kinetic energy and potential energy against $R/R_{cs}$ for $q = 0.01$.

## 7. Distortion of Streamlines and Isotherms

Fluid motion is characterized by a stream function $(\Psi)$ derived from the velocity components $v$ and $w$. The relationship between the stream function $\Psi$ and the velocity components $v$ and $w$ in a two-dimensional flow can be expressed as follows:

$$v = -\frac{\partial \Psi}{\partial Z} \quad \text{and} \quad w = \frac{\partial \Psi}{\partial Y},$$

resulting in a single equation. The arbitrary constants of integration are eliminated by applying the following boundary conditions for $\Psi$ [17]:

$$\Psi = \nabla^2\Psi = 0 \quad \text{for} \quad Y = 0, \sqrt{2}\pi/a \text{ and } Z = 0, 1.$$

Snapshots of the flow field and heat transfer near the onset of steady-state convection are plotted in the form of streamlines and isotherms, respectively, for various values of $R$ and $E$. To find the absolute minimum or absolute maximum values of $\Psi(Y, Z)$, all of the critical points are initially calculated; then, each critical point is examined using sufficient conditions to decide whether $\Psi$ has an absolute minimum or absolute maximum value at this point. It is assumed that $\Psi$ is continuous and possesses first- and second-order partial derivatives at a point $P(a, b)$. If $P$ is a critical point, then $P(a, b)$ is a point of

$$\text{absolute minimum} \quad \text{if} \quad r\tau - s^2 > 0 \quad \text{and} \quad r > 0, \tag{65}$$

$$\text{absolute maximum} \quad \text{if} \quad r\tau - s^2 > 0 \quad \text{and} \quad r < 0, \tag{66}$$

where

$$r = \Psi_{YY}(a, b),\ s = \Psi_{YZ}(a, b) \text{ and } \tau = \Psi_{ZZ}(a, b).$$

No conclusion about an extremum can be drawn if $r\tau - s^2 = 0$, in which case further investigation is needed. If $r\tau - s^2 < 0$, then $\Psi$ has no absolute minimum or absolute maximum at this point, in which case $P(a, b)$ is called a saddle point.

A parametric investigation was carried out to examine how the Rayleigh number ($R$) and Ekman number ($E$) affect the fluid flow and temperature distribution, as shown in Figures 6–8. Figure 6 illustrates the impact of $E$ on the streamlines and isotherms near the critical Rayleigh number ($R_{cs}$). In Figure 6a, the streamlines for $E$ = 0.03 and $q = 0.01$ reveal that the absolute maximum and minimum values of the circulation strength are 0.4155 and 0.41549, respectively. Figure 6c presents the streamlines for $E$ = 0.07 and $q = 0.01$, showing a reduction in the absolute maximum and minimum circulation intensities to $-0.00998$ and $-0.01002$, respectively. Both subfigures in Figure 6a,c indicate that the streamlines exhibit concentric rolling patterns at $R \simeq R_{cs}$. The temperature distribution is represented in Figure 6b,d with isotherms at $R \simeq R_{cs}$. The viscous forces near the onset are comparable to the buoyant forces, and give rise to conduction modes of heat transfer. As $E$ increases from 0.03 to 0.07 (Figure 6b,d), the isotherm remains smooth because the viscous force begins to dominate the buoyant force.

Figure 7 illustrates the impact of the Rayleigh number on the fluid flow and temperature distribution for a fixed Ekman number (=0.03). Figure 7a,b presents the streamlines and isotherms for $R = 2R_{cs}$. It is evident from the figure that the primary parallel rolls are slightly inclined to the right, with maximum and minimum circulation strengths of 1.37693 and $-1.37692$, respectively. The isotherms exhibit wavy patterns, indicating that buoyant forces are beginning to dominate over viscous forces, marking the onset of convective heat transfer. Figure 7c,d depicts the streamlines and isotherms for $R = 5R_{cs}$. In this case, the tilted primary cell has been altered by the emergence of two additional eddies with a circulation strength of $-0.823$ near the upper left and lower right boundaries. Moreover, two new vortices, referred to as $A$ and $A'$, form within the primary cell, displaying absolute maximum and minimum circulation strengths of 1.920 and $-1.920$, respectively. The corresponding isotherm distribution is shown in Figure 7d, which illustrates the convective mode of temperature distribution in the liquid layer. Notably, in Figure 7e,f the primary streamline cell, with maximum and minimum values of 6.20542 and $-6.20541$, is observed to have split into two counter-clockwise rotating cells, labeled $B$ and $B'$. This change occurs as the buoyant force becomes significantly stronger relative to the viscous force. Under these conditions, convection-driven fluid motion is present between the two horizontal plates, with most of the temperature being transferred from the bottom plate to the top plate. As the Rayleigh number increases from $2R_{cs}$ to $8R_{cs}$, the strength of fluid circulation

increases significantly and the temperature gradient between two plates is steep, as can be observed from the streamlines and temperature contours.

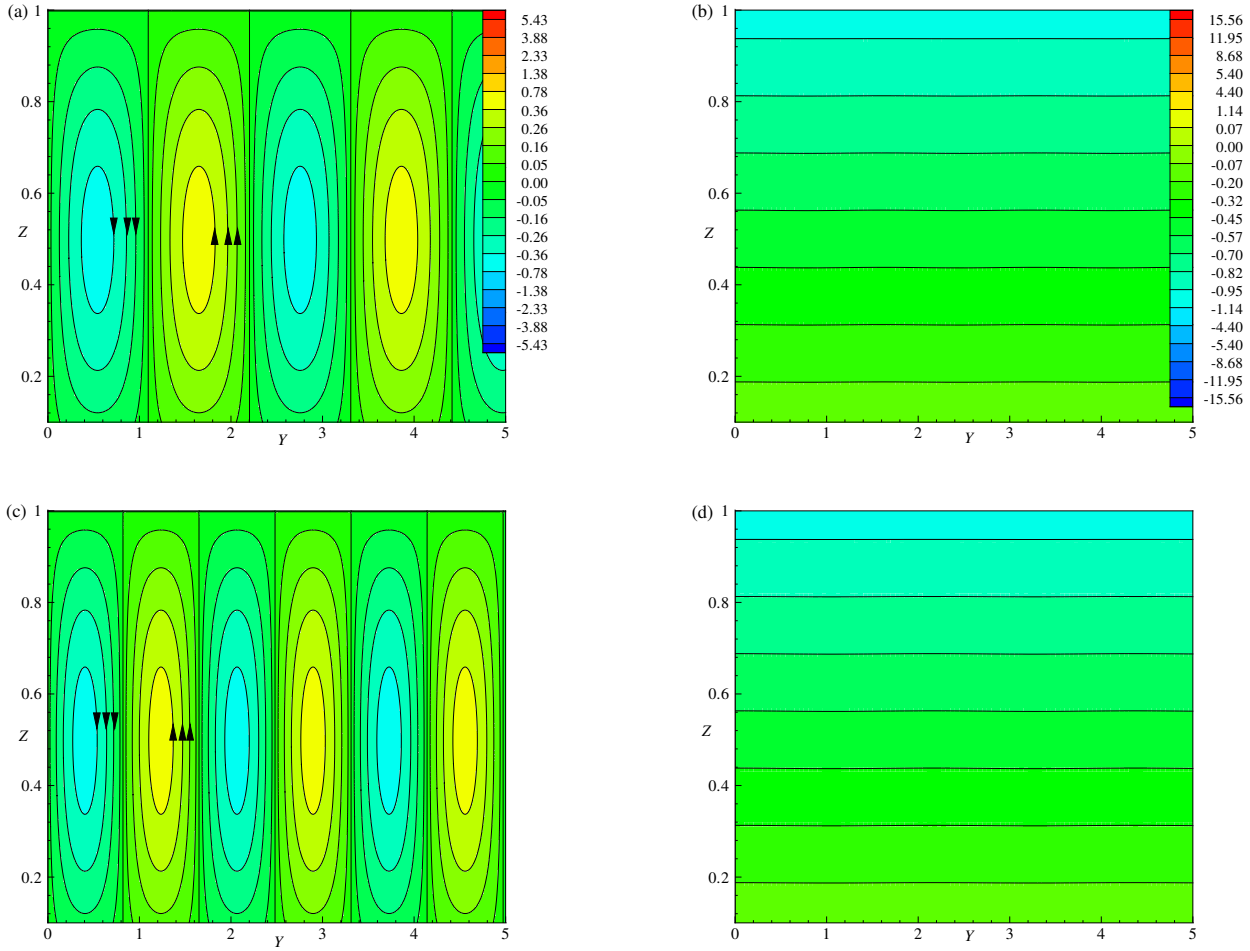


**Figure 6.** The effect of $E$ near $R_{cs}$ and $q = 0.01$: streamlines are plotted for (**a**) $E$ = 0.03 and (**c**) $E$ = 0.07 and isotherms for (**b**) $E$ = 0.03, $R_{cs} = 5262.664915$ and (**d**) $E$ = 0.07, $R_{cs} = 6755.126806$.

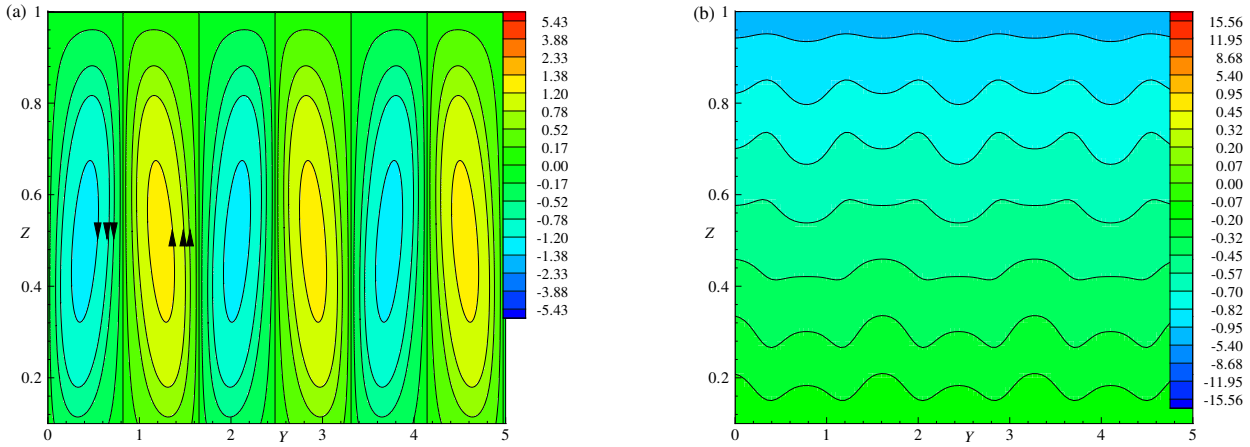


**Figure 7.** *Cont.*

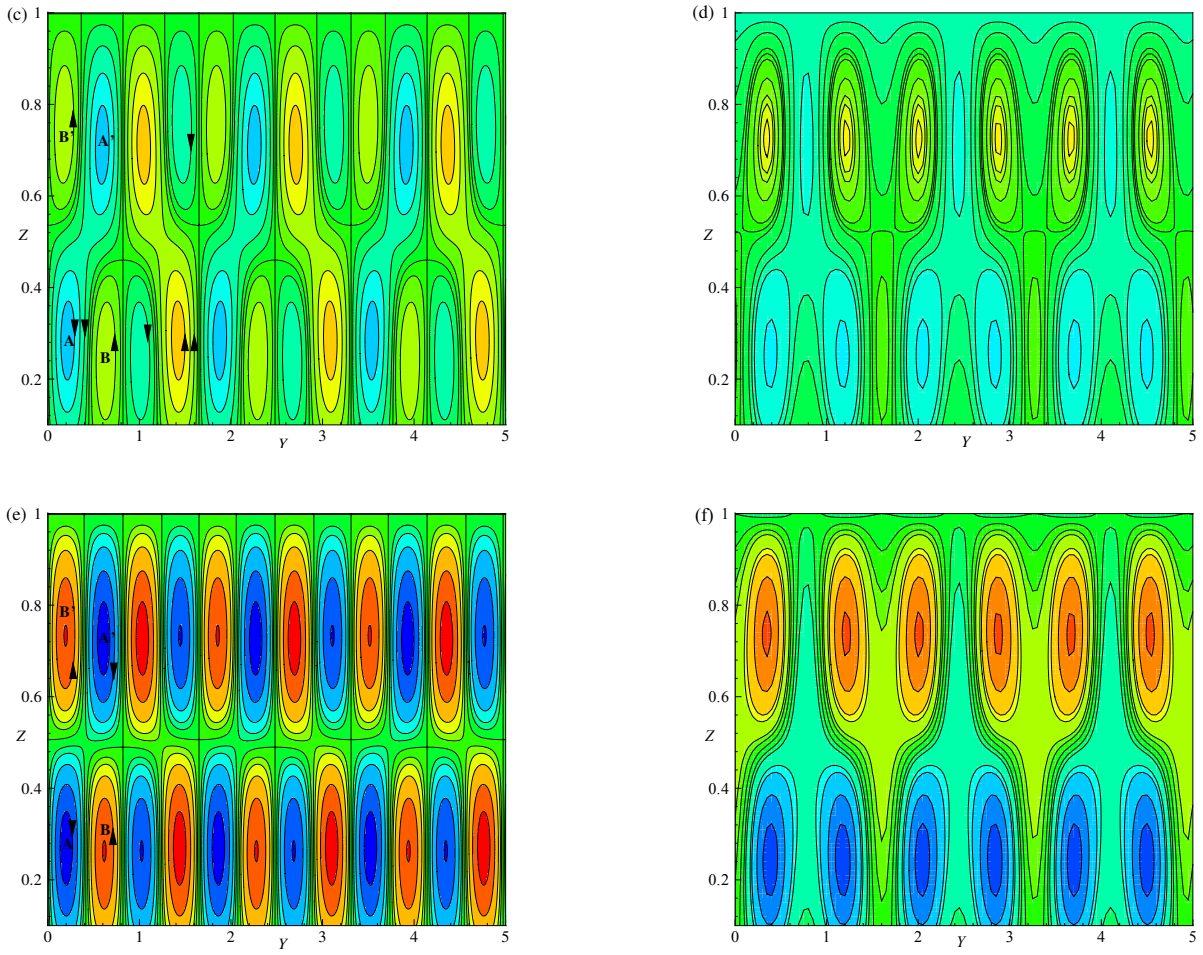


**Figure 7.** The effect of $R = 2R_{cs}, 5R_{cs}, 8R_{cs}$: streamlines (**a**,**c**,**e**) and isotherms (**b**,**d**,**f**) are plotted for $E$ = 0.03, $R_{cs} = 5262.664915$, and $q$ = 0.01.

Figure 8 highlights the effects of viscous forces on streamlines and isotherms for fixed parameters of $R = 8R_{cs}$ and $q = 0.01$. The influence of the Ekman number ($E$) is illustrated by a series of flow patterns, shown in Figures 7e,f and 8a–d for $E$ values of 0.03, 0.05, and 0.07. In Figure 8a, the streamlines for $E = 0.05$ are depicted within the range of $0 \leq Y \leq 1$. The maximum and minimum circulation strengths are measured at 6.07826 and $-6.07805$, respectively. This figure reveals two vortices, labeled $B$ and $B'$, located near the upper left and lower right boundaries, each exhibiting a circulation strength of 3.879. The primary cell is also subdivided into two additional vortices, named $A$ and $A'$. Figure 8c, representing $E$ = 0.07, shows absolute maximum and minimum circulation strengths of 5.95964 and $-5.95926$, respectively. In the range of $0 \leq Y \leq 1$, the flow pattern appears distorted due to the presence of vortices $B$ and $B'$, which are situated near the top and bottom boundaries with a circulation strength of 3.778. Temperature distributions are shown in Figure 8b,d through isotherms for $E$ = 0.05 and 0.07, respectively. Overall, Figure 7e,f and Figure 8 indicate a decline in both the circulation strength of the primary cell and the intensity of the temperature distribution as the Ekman number increases. It is noteworthy that the dominance of the left counterclockwise rotating cell over the right clockwise rotating cell becomes more pronounced as the Ekman number decreases. This phenomenon is attributed to the increase in circulation strength of the right cell, which rises from 3.778 at $E = 0.07$ to 3.879 at $E = 0.05$. The enhanced circulation strength in the right cell suggests that reduced viscous effects allow for more vigorous flow patterns, reinforcing the dominance of the left cell as the Ekman number decreases.

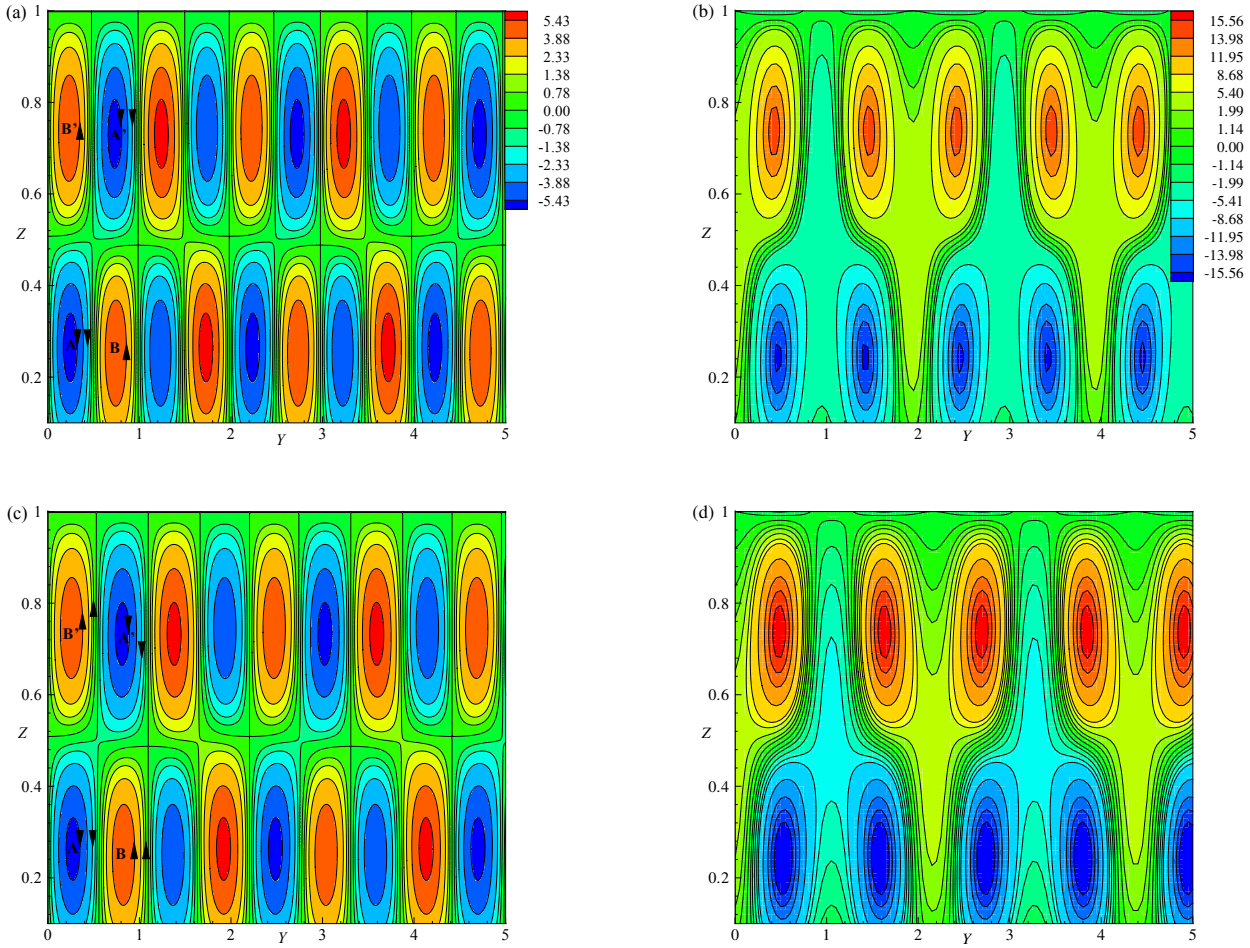


**Figure 8.** The effect of $E$ = 0.05, $R_{cs}$ = 5896.136279, and $E$ = 0.07, $R_{cs}$ = 6755.126806: streamlines (**a**,**c**) and isotherms (**b**,**d**) are plotted for $R = 8R_{cs}$ and $q = 0.01$.

*Topology of Flow*

Topological fluid mechanics focuses on finding the structural characteristics of a fluid flow. This often begins with identifying crucial places in the flow where the vorticity may be zero, then studying the structure of the flow in the vicinity of these spots. The topology constraint of the flow relies on the Euler number, denoted by $\zeta'$. According to Jana et al. [32], $\zeta'$ on the surface is calculated by summing the Poincare indices at 'stagnation points' where the fluid is instantaneously at rest. The number of critical points are related by Euler's identity:

$$NE - (NH + \frac{1}{2}NP) = \zeta', \tag{67}$$

where $NE$ refers to the count of elliptic points, $NH$ signifies the count of hyperbolic points, and $NP$ denotes the count of parabolic points [33,34]. This is the most straightforward outcome of a topological character for a flow, and it remains true throughout the fluid flow. Figure 9 illustrates the vorticity contours for different values of $R$ and fixed $E = 0.03$ and $q = 0.01$. The vorticity contours for $R \simeq R_{cs}$ are illustrated in Figure 9a with $NE = 2$, $NH = 2$ and $NP = 0$. Figure 8b represents the vorticity contours for $R = 8R_{cs}$ with $NE$ = 8, $NH$ = 8 and $NP$ = 0. From Figure 9a,b, we can conclude that the topological relation specified in Equation (67) is satisfied.

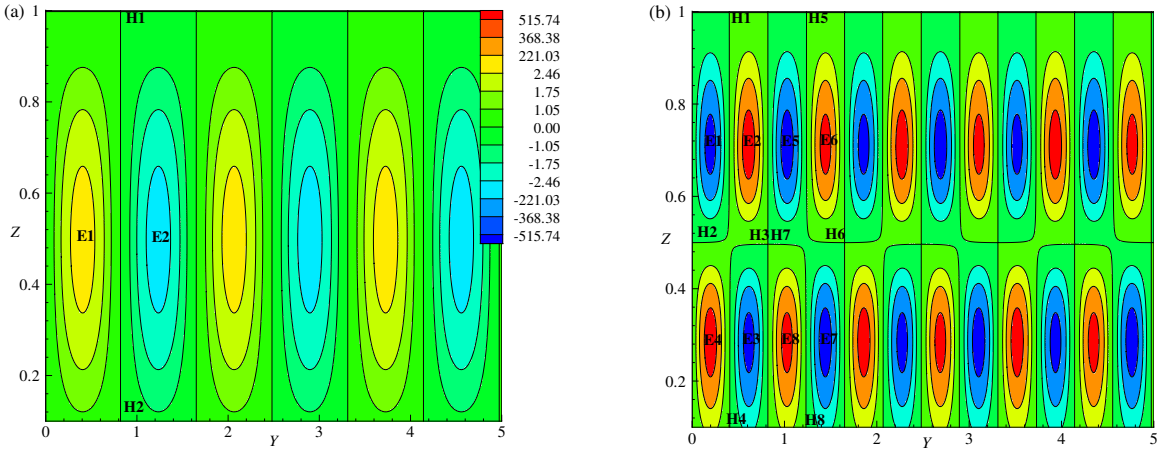


**Figure 9.** Vorticity lines for $E = 0.03$, $R_{cs} = 5262.664915$, and $q = 0.01$: (**a**) $R \simeq R_{cs}$ and (**b**) $R = 8R_{cs}$.

## 8. Heatfunction

The heatline concept is similar to a streamline, except that it visualizes net energy flow in a convection or conduction heat transfer scenario. The visualization of heat transmission through fluid flow was revolutionized by Kimura and Bejan [18] with the introduction of the idea of heatlines. Building upon this breakthrough, Morega and Bejan [35] effectively applied the concept of heatlines. Several researchers [36–43] have applied this concept to various natural convection systems. The heat function ($H^*$) is defined as

$$\frac{\partial H^*}{\partial Y} = wT - \frac{\partial T}{\partial Z}, \tag{68}$$

$$-\frac{\partial H^*}{\partial Z} = vT - \frac{\partial T}{\partial Y}, \tag{69}$$

where $T = T_s + \theta$ and $T_s = T_o - Z$, with $T_0$ as the reference temperature. Differentiating Equations (68) and (69) with respect to $Y$ and $Z$, respectively, then subtracting the two results yields the following equation:

$$\frac{\partial^2 H^*}{\partial Y^2} + \frac{\partial^2 H^*}{\partial Z^2} = \frac{\partial (wT)}{\partial Y} - \frac{\partial (vT)}{\partial Z}. \tag{70}$$

The boundary conditions on $H^*$ can be deduced from the Equations (68) and (69), which define the heat function [30]:

$$H^*(Y,0) = H^*(0,0) + \int_0^Y \left( wT - \frac{\partial T}{\partial Z} \right) dY, \text{ at } Z = 0 \text{ and } 0 \le Y \le \sqrt{2}\pi/a, \tag{71}$$

$$H^*(Y,1) = H^*(0,1) + \int_0^Y \left( wT - \frac{\partial T}{\partial Z} \right) dY, \text{ at } Z = 1 \text{ and } 0 \le Y \le \sqrt{2}\pi/a, \tag{72}$$

$$H^*(0,Z) = H^*(0,0) - \int_0^Z \left( vT - \frac{\partial T}{\partial Z} \right) dZ, \text{ at } Y = 0 \text{ and } 0 \le Z \le 1, \tag{73}$$

$$H^*(\sqrt{2}\pi/a,Z) = H^*(\sqrt{2}\pi/a,0) - \int_0^Z \left( vT - \frac{\partial T}{\partial Z} \right) dZ, \text{ at } Y = \sqrt{2}\pi/a \text{ and } 0 \le Z \le 1. \tag{74}$$

*Results and Discussion for Heatlines*

Figure 10a–d depicts the net energy flow through convection and conduction at various Rayleigh numbers ($R$) while keeping the Ekman number constant at ($E = 0.03$). For $R < R_{cs}$, conduction primarily governs the heat transfer across the layer. In Figure 10a, we observe the heat transfer when $R \simeq R_{cs}$, with absolute maximum and minimum values of the heatlines recorded at 6.32101 and $-0.07152$, respectively, within the range of $0 \leq Y \leq 5$. This indicates that nonlinear heat transfer begins to take place at $R \simeq R_{cs}$, marking a transition from conduction to convection. At this point, the heat transfer across the horizontal layer remains low due to weak buoyancy forces. Figure 10b shows the results for $R = 1.05R_{cs}$, where the absolute maximum and minimum values of the heatlines are 6.34066 and $-0.2862$, respectively. The influence of increased convection is more evident in the heatlines. As $R$ increases from $R_{cs}$ to $1.05R_{cs}$, the previously curved heatlines transform into closed loops, as illustrated in Figure 10b. With a further increase in the Rayleigh number to $R = 1.15R_{cs}$, the absolute maximum and minimum heatline values are 6.36755 and $-0.50782$, respectively, as shown in Figure 10c. The maximum value of 6.36755 signifies a further enhancement in heat transfer at $R = 1.15R_{cs}$. Finally, Figure 10d presents data for $R = 1.15R_{cs}$, displaying absolute maximum and minimum values of 6.38648 and $-0.60663$, respectively. Here, convection intensifies and becomes the dominant mechanism for heat transfer. A significant number of heatlines appear near the hot wall, signifying a high heat flux toward the cold wall as $R$ increases. This clearly illustrates the critical role that convection plays in the heat transfer process as the Rayleigh number continues to rise.

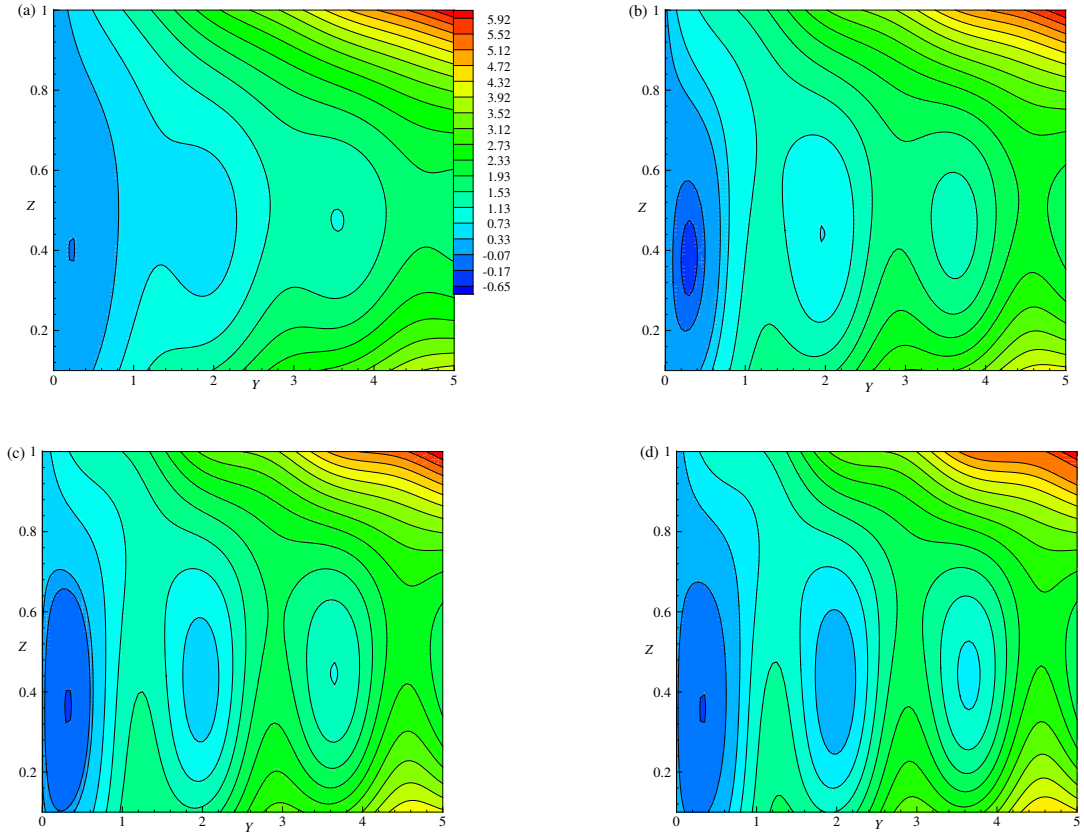


**Figure 10.** The effect of $R \simeq R_{cs}$, $R = 1.05R_{cs}$, $1.15R_{cs}$, and $1.25R_{cs}$: heatlines (**a**–**d**) are plotted for $E = 0.03$ and $R_{cs} = 5262.664915$, $T_0 = 1$, and $q = 0.01$, respectively.

Figures 10d and 11a,b demonstrate the impact of the Ekman number $E$ on the heat transfer for a fixed ratio $R = 1.25R_{cs}$. In Figure 11a, with $E = 0.05$, the heatlines exhibit absolute maximum and minimum values of 5.92779 and $-0.66694$, respectively. Conversely, Figure 11b for $E = 0.07$ shows maximum and minimum values of 4.3253 and $-0.65158$, respectively, indicating that both the magnitude and number of closed loops in the heatlines decrease within the range of $0 \leq Y \leq 5$ as $E$ increases. Increasing $E$ correlates with a reduction in both the magnitude and number of closed loops in the heatlines. This suggests that higher Ekman numbers, which are associated with more significant viscous forces, diminish the effectiveness of convective heat transfer. Moreover, analysis of Figures 10d and 11a,b indicates that the highest heatline values observed in the corner region increase as $E$ decreases. This further reinforces the idea that lower Ekman numbers are linked to improved heat flow, highlighting the critical role of viscous effects in influencing the efficiency of convective heat transfer in the studied system. This can be attributed to the lower viscosity of the fluid at smaller Ekman numbers, which enhances the convective flow and facilitates more effective heat transfer.

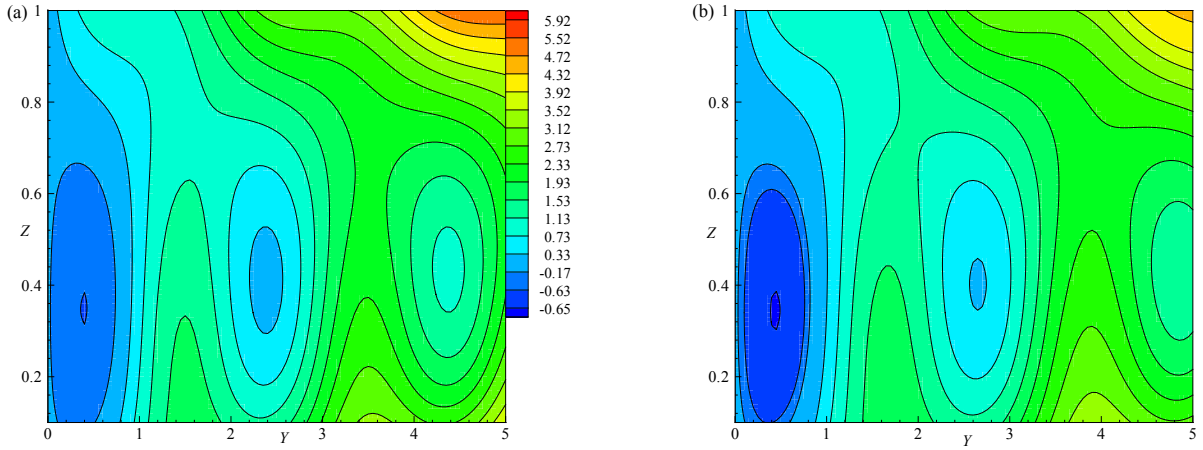


**Figure 11.** The effect of $E = 0.05$, $R_{cs} = 5896.136279$, $E = 0.07$, and $R_{cs} = 6755.126806$: heatlines (**a**,**b**) are plotted for $R = 1.25R_{cs}$, $T_0 = 1$, and $q = 0.01$.

## 9. Total Entropy Generation

It is essential to grasp how to use energy resources efficiently while minimizing energy degradation, particularly in terms of reducing entropy generation during heat transfer. This study connects entropy generation to the irreversible aspects of heat transfer and the viscous effects that occur within the fluid and at the interfaces between the fluid and solid surfaces. The total nondimensional entropy generation rate, denoted as ($S_{gen}$), is determined by summing the contributions from heat transfer irreversibility ($S_{HTI}$) and fluid friction irreversibility ($S_{FFI}$). This methodology draws upon the approaches outlined in references [44–48]. The total entropy generation can be expressed mathematically as follows:

$$S_{gen} = S_{HTI} + S_{FFI}, \tag{75}$$

$$S_{HTI} = \left(\frac{\partial T}{\partial Y}\right)^2 + \left(\frac{\partial T}{\partial Z}\right)^2, \tag{76}$$

$$S_{FFI} = \chi\left[2\left(\frac{\partial v}{\partial Y}\right)^2 + 2\left(\frac{\partial w}{\partial Z}\right)^2 + \left(\frac{\partial v}{\partial Z} + \frac{\partial w}{\partial Y}\right)^2\right]. \tag{77}$$

In this study, the nondimensional velocity and temperature functions, referred to as $v$, $w$, and $T$, are discussed in Section 2, with the magnetic permeability parameter $\chi$ (magnetic

permeability) fixed as $10^{-4}$. The viscous dissipation model proposed by Baytas [49] serves as the foundation for deriving Equation (75). A parametric investigation has been carried out to assess how the Rayleigh number ($R$) and Ekmann number ($E$) influence local entropy generation. Figure 12a–d illustrates the local entropy generation related to heat transfer and fluid friction for various values of $R$. It can be observed that at lower $R$ values, the maximum entropy generation remains relatively low due to limited heat transfer and fluid motion. This phenomenon occurs because the weak buoyancy forces at low $R$ lead to a regime in which heat transfer is primarily conductive. In contrast, Figure 12b–d reveals that as $R$ increases, the total entropy generation associated with heat transfer also rises, particularly in the vicinity of the hot plate. This observation indicates that enhanced buoyancy forces improve the convective heat transfer mechanism. Additionally, Figure 13a,b demonstrates that as the Ekman number $E$ increases there is a corresponding increase in total entropy generation due to fluid friction, highlighting the relationship between viscous effects and entropy generation within the system. This increase can be attributed to the fact that entropy generation due to fluid friction is dependent on the velocity gradient, which in turn is influenced by the magnetic permeability of the fluid.

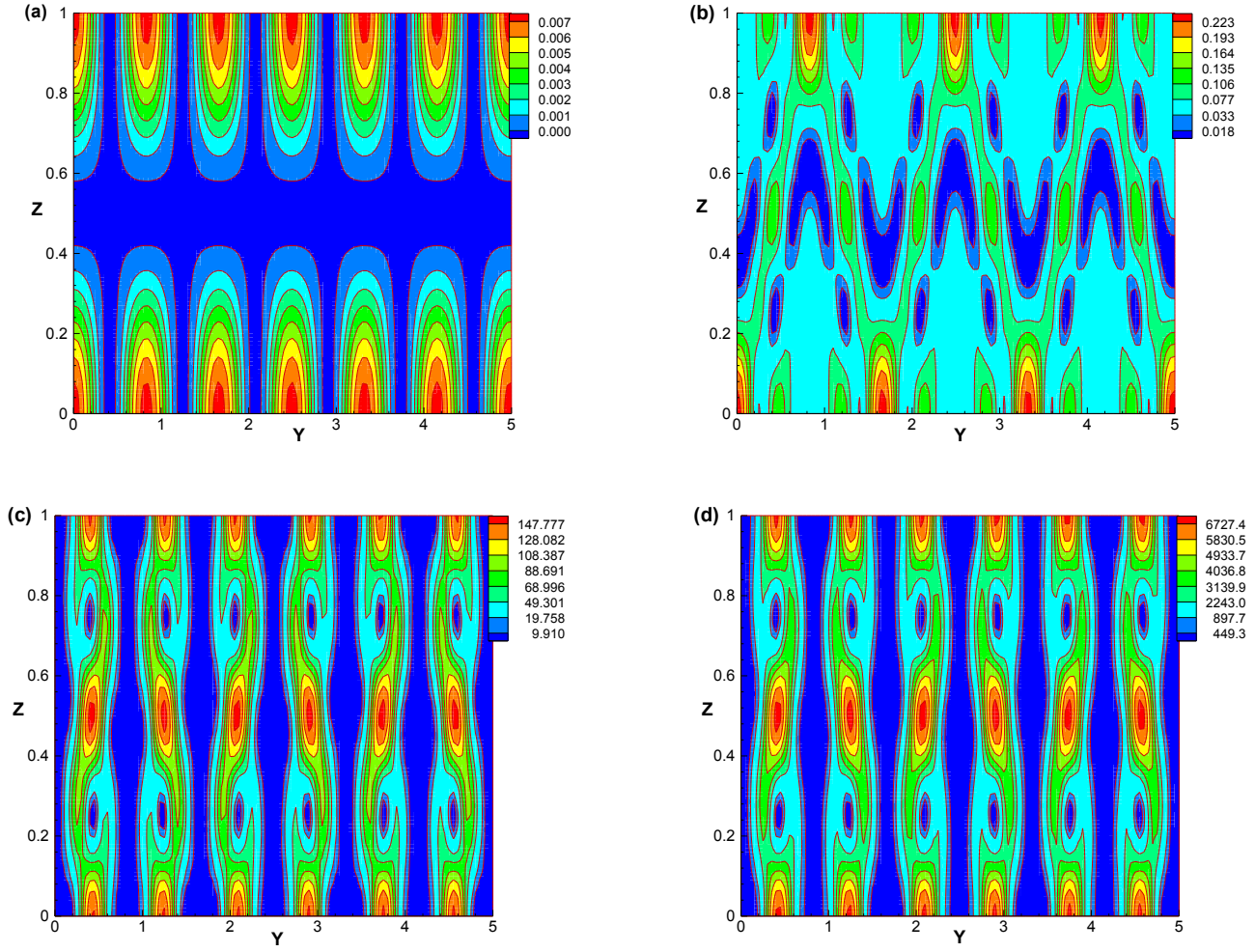


**Figure 12.** Total entropy generation due to heat transfer and fluid flow for $E = 0.03$. $R_{cs} = 5262.664915$, and $q = 0.01$: (**a**) $R \simeq R_{cs}$, (**b**) $R = 2R_{cs}$, (**c**) $5R_{cs}$, and (**d**) $8R_{cs}$.

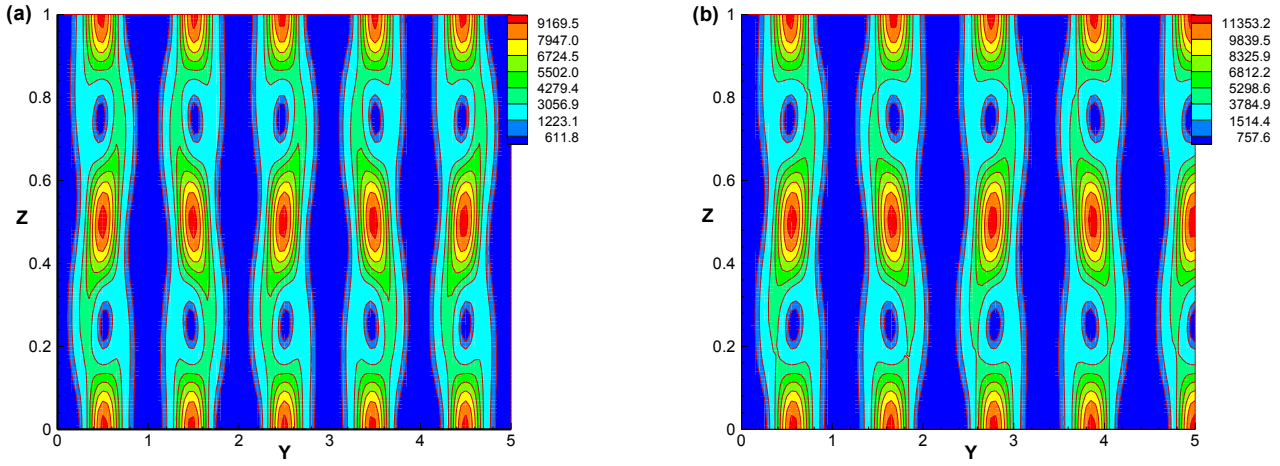


**Figure 13.** Total entropy generation due to heat transfer and fluid flow for $R = 8R_{cs}$ and $q = 0.01$: (**a**) $E = 0.05$, $R_{cs} = 5896.136279$ and (**b**) $E = 0.07$, $R_{cs} = 6755.126806$.

## 10. Conclusions

In this research, we have analytically examined the Rayleigh–Bénard system involving an electrically conducting fluid that rotates around a vertical axis while exposed to a uniform horizontal magnetic field. Our detailed analysis focused on fluid flow patterns, temperature distribution, and heat transfer mechanisms, utilizing streamlines, isotherms, and heatlines for visualization. This approach enhances our understanding of heat flow dynamics in the Earth's liquid core, particularly when the flow rolls align with the magnetic field. We found that when the Rayleigh number ($R$) surpasses the critical threshold $R > R_{cs}$, convection becomes the dominant heat transfer mode, driven by substantial heat flow from the bottom of the layer. Below, we highlight some significant outcomes of our study:

- Linear stability analysis revealed that as the Ekman number ($E$) decreases, the critical Rayleigh number ($R_{cs}$) also decreases, indicating that lower $E$ values stabilize the system.
- The nonlinear partial differential equations were solved using the perturbation method up to $O(\epsilon^8)$ yielding approximate solutions for the system.
- Analysis of the local Nusselt number indicated that its maximum value increases with rising Rayleigh number ($R$).
- As $E$ decreases, the number of peaks in the local Nusselt number ($N_L$) increases.
- From the results of the Nusselt number, it is observed that heat flux increases as $E$ decreases.
- A decrease in $E$ corresponds to an increase in the total energy of the system.
- Based on the trajectories of heatlines, streamlines, and isotherms, it was determined that decreasing $E$ leads to greater deformation of the flow field and enhanced heat transfer with increased rotation.
- At higher Rayleigh numbers, the primary source of entropy generation is attributed to irreversible heat transfer; conversely, at high Ekman numbers, irreversibility arises from fluid friction.

To further expand on these findings, we recommend the following avenues for future research:

- Three-Dimensional Nonlinear Analysis: Future studies should explore three-dimensional nonlinear analyses of the system. While our current analysis is based on two-dimensional models, three-dimensional effects can significantly influence flow patterns, stability, and heat transfer. Investigating the interplay between axial and radial components of the flow may yield richer dynamics and insights into the complexities of the thermal system.
- Oscillatory Convection: Incorporating oscillatory convection into the study will provide a deeper understanding of how time-dependent flow can affect heat transfer

mechanisms. Oscillatory convection can occur due to various external influences, such as periodic heating or fluid motion, and examining its impact could reveal important behaviors in fluid dynamics and thermal transport, particularly in systems subjected to fluctuating thermal gradients.

**Author Contributions:** Conceptualization, G.S. and Y.R.; Methodology, Y.R.; Software, D.L.; Validation, Y.R., G.S. and D.L.; Visualization G.S.; Writing—Original Draft Preparation, G.S.; Writing—Review and Editing, Y.R., G.S. and D.L.; Funding Acquisition, D.L.; Project Administration, D.L. All authors have read and agreed to the published version of the manuscript.

**Funding:** D.L. acknowledges the partial financial support from Centers of Excellence with BASAL/ANID financing, Grant ABF220001.

**Data Availability Statement:** The original contributions presented in the study are included in the article, further inquiries can be directed to the corresponding author.

**Conflicts of Interest:** The authors declare no conflicts of interest.

## Nomenclature

The following abbreviations are used in this manuscript:

| | |
|---|---|
| $A$ | Amplitude |
| $\vec{B}$ | Magnetic field |
| $\vec{B}_s$ | Static magnetic field |
| $B_0$ | Characteristic field strength |
| $a$ | Wavenumber |
| $p$ | Pressure |
| $E$ | Ekman number |
| $\overrightarrow{1_Z}$ | Unit vector along Z-axis |
| $\overrightarrow{1_Y}$ | Unit vector along Y-axis |
| $q$ | Ratio of thermal and magnetic diffusivities |
| $d$ | Convective zone depth |
| $\vec{g}$ | Gravitational field |
| $H^*$ | Heatfunction |
| $Nu$ | Average Nusselt number |
| $R$ | Rayleigh number |
| $R_{cs}$ | Critical Rayleigh number for stationary convection |
| $T$ | Temperature |
| $T_s$ | Static temperature |
| $\overrightarrow{V_s}$ | Static velocity |
| $T_0$ | Reference temperature |
| $\Delta T$ | Temperature difference between top and bottom layers |
| $t$ | Time |
| $\vec{V}$ | Velocity vector |
| $u, v, w$ | Velocity components |
| $X, Y, Z$ | Cartesian coordinates |
| $RBC$ | Rayleigh-Bénard Convection |
| ***Greek symbol*** | |
| $\Lambda$ | Elsasser number |
| $\beta$ | Adverse temperature gradient |
| $\theta$ | Perturbed temperature |
| $\eta$ | Magnetic diffusivity |
| $\rho$ | Density |
| $\rho_0$ | Reference density |
| $\kappa$ | Thermal diffusivity |
| $\nu$ | Kinematic viscosity |
| $\alpha$ | Thermal expansion coefficient |
| $\mu$ | Dynamic viscosity |
| $\mu_m$ | Magnetic permeability |

| | |
|---|---|
| $\Omega$ | Angular velocity |
| $\lambda$ | Growth rate |
| ***Superscript*** | |
| $'$ | Dimensional form |
| * | Perturbed quantities |

## References


1. Chandrasekar, S. *Hydrodynamic and Hydromagnetic Stability*; Oxford Clarendon Press: Oxford, UK, 1961.
2. Roberts, P.H.; Jones, C.A. The onset of magnetoconvection at large Prandtl number in a rotating layer 1. Finite magnetic diffusion. *Geophys. Astrophys. Fluid Dyn.* **2000**, *92*, 289–325. [CrossRef]
3. Eltayeb, I.A. Hydromagnetic convection in a rapidly rotating fluid layer. *Proc. R. Soc. Lond. A* **1972**, *326*, 229–254.
4. Childress, S.; Soward, A.M. Convection-Driven Hydromagnetic Dynamo. *Phys. Rev. Lett.* **1972**, *29*, 837. [CrossRef]
5. Soward, A.M. Convection Driven Dynamos. *Phys. Earth Planet. Inter.* **1979**, *20*, 134–151. [CrossRef]
6. Braginsky, S.I. Magnetic Waves in the Core of the Earth. *Geophys. Asirophys.* **1980**, *14*, 189–208. [CrossRef]
7. Gary, A.; Paul, G.; Roberts, H. A three-dimensional convective dynamo solution with rotating and finitely conducting inner core and mantle. *Phys. Earth Planet. Inter.* **1995**, *91*, 63–75.
8. Jones, C.A.; Roberts, P.H. Convection-driven dynamos in a rotating plane layer. *J. Fluid Mech.* **2000**, *404*, 311–343. [CrossRef]
9. Taylor, J.B. The Magneto-Hydrodynamics of a Rotating Fluid and the Earth's Dynamo Problem. *Proc. R. Soc. Lond. A* **1963**, *274*, 274–283.
10. Soward, A.M. Finite-amplitude thermal convection and geostrophic flow in a rotating magnetic system. *J. Fluid Mech.* **1980**, *98*, 449–471. [CrossRef]
11. Geiger, G.; Busse, F. On the Onset of Thermal Convection in Slowly Rotating Fluid Shells. *Geophys. Asrrophys. Fluid Dyn.* **1981**, *18*, 147–156. [CrossRef]
12. Matthews, P.C. Dynamo action in simple convective flows. *R. Soc. Lond. A* **1999**, *455*, 1829–1840. [CrossRef]
13. Kono, M.; Roberts, P.H. Definition of the Rayleigh number for geodynamo simulation. *Phys. Earth Planet. Inter.* **2001**, *128*, 13–24. [CrossRef]
14. Cattaneo, F.; Hughes, D.W. Dynamo action in a rotating convective layer. *J. Fluid Mech.* **2006**, *553*, 401–418. [CrossRef]
15. Roberts, P.H.; Kono, M. Gravitational energy release in an evolving Earth model. *Earth Planets Space* **2007**, *59*, 651–659. [CrossRef]
16. Tilgner, A. Transitions in Rapidly Rotating Convection Driven Dynamos. *Phys. Rev. Lett.* **2012**, *109*, 248–501. [CrossRef]
17. Kuo, H.L. Solution of the non-linear equations of the cellular convection and heat transport. *J. Fluid Mech.* **1960**, *10*, 611–630. [CrossRef]
18. Kimura, S.; Bejan, A. The heatline visualization of convective heat transfer. *J. Heat Transf.* **1983**, *105*, 916–919. [CrossRef]
19. Rameshwar, Y.; Srinivas, G.; Laroze, D. Nonlinear analysis of cross rolls of electrically conductiong fluid under an applied magnetic field with rotation. *Processes* **2023**, *11*, 1945. [CrossRef]
20. Khedher, N.B.; Ullah, Z.; Alturki, M.; Mirza, C.R.; Eldin, S.M. Effect of joul heating and MHD on periodical analysis of current density and amplitude of heat transfer of electrically conducting fluid along thermal magnetized cylinder. *Ain Shams Eng. J.* **2024**, *15*, 102–374.
21. Li, S.; Faizan, M.; Ali, F.; Ramasekhar, G.; Muhammad, T.; El-Wahed Khalifa, H.A.; Ahmad, Z. Modelling and analysis of heat transfer in MHD stagnation point flow of Maxwell nanofluid over a porous rotating disk. *Alex. Eng. J.* **2024**, *91*, 237–248. [CrossRef]
22. Shamshuddin, M.D.; Anwar, S.; Kanayo Kenneth, A.; Usman; Wasim, J. A semi-analytical approach to investigate the entropy generation in a tangent hyperbolic magnetized hybrid nanofluid flow upon a stretchable rotating disk. *J. Magn. Magn. Mater.* **2023**, *574*, 170–664. [CrossRef]
23. Assiri, T.A.; Bilal, M.; Mahmoud, E.E.; Ali, A.; Asamoah, J.K.K.; Adnan. Numerical investigation of forced convective MHD tangent hyperbolic nanofluid flow with heat source/sink across a permeable wedge. *AIP Adv.* **2024**, *14*, 65–302. [CrossRef]
24. Ramanuja, M.; Muni Sarala, G.; Kavitha, J.; Srinivasulu, A.; Gopi Krishna, G. A fully developed viscous electrically conducting fluid through infinitely parallel porous plates. *Heat Transf.* 2024, *early view*. [CrossRef]
25. Tang, Q.; Sun, Y.; Li, J.; Zhou, M.; Yang, D.; Pang, Y. Preparations of 25 wt% of Pyraclostrobin Nanosuspension Concentrate (SC) Using Lignosulfonate-Based Colloidal Spheres to Improve Its Thermal Storage Stability. *Molecules* **2024**, *29*, 1419. [CrossRef] [PubMed]
26. Li, J.-X.; Lu, Y.-J.; Quan, K.-Y.; Wu, L.-B.; Feng, X.; Wang, W.-Z. One-pot cocrystallization of mononuclear and 1D cobalt(II) complexes based on flexible triclopyr and 2, 2′ bipyridine coligands: Structural analyses, conformation comparison, non-covalent interactions and magnetic properties. *J. Mol. Struct.* **2024**, *1297*, 136–830. [CrossRef]
27. Wu, Y.-L.; Tang, P.-F.; Zhang, Q.; Yan, Y.-T.; Zhang, S.; Yang, G.-P.; Wang, Y.-Y. Nanoarchitectonics and catalytic performances of metal–organic frameworks supported metal nanoparticles. *Appl. Organomet. Chem.* **2023**, *38*, e7308. [CrossRef]
28. Komori, K.; Kito, S.; Naumara, T.; Inaguma, Y.; Inagai, T. Fluid flow and heat transfer in the transition process of natural convection over an inclined plate. *Heat Trans. Asian Res.* **2001**, *30*, 648–659. [CrossRef]
29. Kimura, F.; Kitamura, K.; Yamaguchi, M.; Asami, T. Fluid flow and heat transfer of natural convection adjacent to upward facing inclined heated plates. *Heat Trans. Asian Res.* **2003**, *32*, 278–291. [CrossRef]

30. Rameshwar, Y.; Rawoof Sayeed, M.A.; Rani, H.P.; Laroze, D. Finite amplitude cellular convection under the influence of a vertical magnetic field. *Int. J. Heat Mass Transf.* **2017**, *114*, 559–577. [CrossRef]
31. Batchelor, G.K. *An Introduction to Fluid Dynamics*; Cambridge University Press: Cambridge, UK, 1993.
32. Jana, S.C.; Metcalfe, G.; Ottino, J.M. Experimental and computational studies of mixing in complex Stokes flows: The vortex mixing flow and multicellular cavity flows. *J. Fluid Mech.* **1994**, *269*, 199–249. [CrossRef]
33. Tony Sheu, W.H.; Rani, H.P. Exploration of vortex dynamics for transitional flows in a three-dimensional backward facing step channel. *J. Fluid Mech.* **2006**, *550*, 61–83. [CrossRef]
34. Sheu, T.; Rani, H.P.; Ten-China, T.; Tsai, S.F. Multilple states, topology and bifurcations of natural convection in a cubical cavity. *Comput. Fluids* **2008**, *37*, 1011–1028. [CrossRef]
35. Morega, A.I.; Bejan, A. Heatline visualization of forced convection laminar boundry layers. *Int. J. Heat Mass Transf.* **1993**, *36*, 3957–3966. [CrossRef]
36. Bejan, A. *Convection Heat Transfer*; Wiley: New York, NY, USA, 1984; pp. 21–23.
37. Morega, A.I.M. Magnetic field influence on the convective heat transfer in the solidification processes. *Rev. Roum. Sci. Tech. Electrotechnol. Energy* **1988**, *33*, 155–166.
38. Nield, D.A.; Bejan, A. *Convection in Porous Media*, 2nd ed.; Springer: New York, NY, USA, 1999.
39. Costa, V.A.F. Bejan's heatlines and masslines for convection visualization and analysis. *Appl. Mech. Rev.* **2006**, *59*, 26–145. [CrossRef]
40. Basak, T.; Roy, S. Role of Bejan's heatlines in heat flow visualization and optimal thermal mixing for differentially heated square enclosures. *Int. J. Heat Mass Transfer.* **2008**, *51*, 3486–3503. [CrossRef]
41. Basak, T.; Roy, S.; Matta, A.; Pop, I. Analysis of heatlines for natural convection within porous trapozoidal cnclosure: Effect of uniform and non-uniform heating of bottom wall. *Int. J. Heat Mass Transfer.* **2010**, *53*, 5947–5961. [CrossRef]
42. Deng, Q.H.; Tang, G.F.; Li, Y. A combined temperature scale for analyzing natural convection in rectangular enclosures with discrete wall heat sources. *Int. J. Heat Mass Transfer.* **2002**, *45*, 3437–3446. [CrossRef]
43. Varol, Y.; Oztop, H.F.; Mobedi, M.; Pop, I. Visualization of heat flow using Bejan's heatline due to natural convection of water near 4 °C in thick walled porous cavity. *Int. J. Heat Mass Transfer.* **2010**, *53*, 1691–1698. [CrossRef]
44. Bejan, A. *Entropy Generation through Heat and Fluid Flow*; Wiley: New York, NY, USA, 1982.
45. Basak, T.; Anandalakshmi, R.; Roy, S.; Pop, I. Role of entropy generation on thermal management due to thermal convection in porous trapezoidal enclosures with isothermal and non-isothermal heating of wall. *Int. J. Heat Mass Trans.* **2013**, *67*, 810–828. [CrossRef]
46. Basak, T.; Das, D.; Biswal, P. Heatlines: Modeling, visualization, mixing and thermal management. *Prog. Energy Combust. Sci.* **2017**, *64*, 157–218. [CrossRef]
47. Al-Hadhrami, A.K.; Elliott, L.; Ingham, D.B. A New Model for Viscous Dissipation in Porous Media across a Range of Permeability Values. *Trans. Porous Med.* **2003**, *53*, 117–122. [CrossRef]
48. Homan, K.; Gurgenci, H. Effects of viscous dissipation and boundary conditions on forced convection in a channel occupied by a saturated porous medium. *Trans. Porous Med.* **2007**, *68*, 301–319. [CrossRef]
49. Baytas, A.C. Entropy generation for natural convection in an inclined porous cavity. *Int. J. Heat Mass Trans.* **2000**, *43*, 2089–2099. [CrossRef]